Multifunctional role of GPCR signaling in epithelial tube formation

Vishakha Vishwakarma, Thao Phuong Le, and SeYeon Chung*

Department of Biological Sciences, Louisiana State University, Baton Rouge, LA 70803, USA

*Author for correspondence: seyeonchung@lsu.edu

Key words: *Drosophila*, Salivary gland, Fog signaling, GPCR, Actomyosin

Running title: GPCR signaling in tube formation

Abstract

Epithelial tube formation requires Rho1-dependent actomyosin contractility to generate the cellular forces that drive cell shape changes and rearrangement. Rho1 signaling is activated by G protein-coupled receptor (GPCR) signaling at the cell surface. During *Drosophila* embryonic salivary gland (SG) invagination, the GPCR ligand Folded gastrulation (Fog) activates Rho1 signaling to drive apical constriction. The SG receptor that transduces the Fog signal into Rho1-dependent myosin activation has not been identified. Here, we reveal that the Smog GPCR transduces Fog signal to regulate Rho kinase accumulation and myosin activation in the apicomedial region of cells to control apical constriction during SG invagination. We also report on unexpected Fog-independent roles for Smog in maintaining epithelial integrity and organizing cortical actin. Our data supports a model wherein Smog regulates distinct myosin pools and actin cytoskeleton in a ligand-dependent manner during epithelial tube formation.

Introduction

The formation of three-dimensional tubes by invagination from flat epithelial sheets is a fundamental process in forming organs, such as lungs and kidneys (Andrew and Ewald, 2010). The *Drosophila* embryonic salivary gland (SG) is a premier model system to study the mechanisms underlying epithelial tube morphogenesis (Chung et al., 2014; Girdler and Röper, 2014). The SG begins as a two-dimensional plate of cells on the embryo surface. Neither cell division nor cell death occurs once the SG cells are specified; all the morphogenetic changes arise by changes in cell shape and rearrangement.

A major cell shape change during SG invagination is apical constriction, wherein the apical side of epithelial cells shrinks while keeping the nearly constant volume (Lubarsky and Krasnow, 2003; Martin and Goldstein, 2014). During stage 11, SG cells begin to invaginate at the dorsal/posterior region of the placode through apical constriction (Fig. 1A). This leads to forming a narrow invagination pit through which all SG cells eventually internalize. Apical constriction is observed in both invertebrates and vertebrates, driving morphogenetic processes ranging from gastrulation in *Drosophila* and *Xenopus* to lens formation in the mouse eye to formation of tubular organs such as the *Drosophila* SG and chicken lungs (Kim et al., 2013; Myat and Andrew, 2000; Plageman et al., 2011; Sweeton et al., 1991). Defects in apical constriction result in defects in overall tissue shape, suggesting that coordinated apical constriction is required for final tissue architecture (Chung et al., 2017; Guglielmi et al., 2015; Izquierdo et al., 2018).

Contractile actomyosin networks generate the cellular forces driving coordinated cell behaviors during epithelial morphogenesis (Gorfinkiel and Blanchard, 2011; Levayer and Lecuit, 2012; Munjal and Lecuit, 2014). Non-muscle myosin II (hereafter referred to as myosin) uses its motor activity to pull on actin filaments anchored to adherens junctions (AJs) to apply tension on the junction and neighboring cells. Three distinct pools of myosin generate the contractile forces required for SG invagination (Booth et al., 2014; Chung et al., 2017; Röper, 2012). Apicomedial myosin forms in the center of the apical side of the SG cell and drives apical constriction (Booth et al., 2014; Chung et

al., 2017; Röper, 2012). Junctional myosin, associated with AJs of SG cells, is involved in cell intercalation (Sanchez-Corrales et al., 2018). A supracellular myosin cable surrounding the entire SG placode generates the tissue-level compressing force (Chung et al., 2017; Röper, 2012). From studies in the past several years by us and others, we are beginning to understand how each myosin pool is created and regulated during SG invagination (Booth et al., 2014; Chung et al., 2017; Le and Chung, 2021; Röper, 2012; Sanchez-Corrales et al., 2018; Sidor et al., 2020).

Localized activation of the RhoA (Rho1 in *Drosophila*) GTPase is key to creating and/or polarizing contractile myosin structures in epithelial cells (Blanchard et al., 2010; Dawes-Hoang et al., 2005; Martin et al., 2009; Mason et al., 2013). Studies in *Drosophila* have identified the Folded gastrulation (Fog) pathway as a key signaling pathway regulating Rho1 signaling during epithelial morphogenesis (Manning and Rogers, 2014). During *Drosophila* gastrulation, two G protein-coupled receptors (GPCRs), Smog (ubiquitously expressed) and Mist (mesoderm-specific), respond to Fog to activate heterotrimeric G proteins, Rho1, and Rho kinase (Rok) to regulate myosin contractility (Costa et al., 1994; Dawes-Hoang et al., 2005; Kerridge et al., 2016; Kölsch et al., 2007; Manning et al., 2013; Mason et al., 2013; Parks and Wieschaus, 1991). In our previous study in the SG, we also revealed a tissue-specific regulation of Fog signaling to activate myosin contractility: the Fork head (Fkh) transcription factor regulates SG upregulation of *fog*, which promotes accumulation of Rok and myosin specifically in the apicomedial region of SG cells to drive clustered apical constriction (Chung et al., 2017; Fig. 1A). Yet, it is unknown how the Fog signal is sensed and transduced into downstream Rho1 signaling during epithelial tube formation.

Studies in early *Drosophila* embryos have suggested a role of GPCR signaling as a common module for Rho1 activation in different subcellular regions of the cell. In the mesoderm, Smog and Mist function together to activate myosin in the apicomedial region of cells to drive apical constriction (Kerridge et al., 2016). In the ectoderm, where no apical constriction occurs, Smog is required for junctional myosin activation to drive cell intercalation (Kerridge et al., 2016). Recent work further has shown that distinct RhoGEFs activate myosin contractility in the apical and junctional domain of epithelial

cells under the control of specific G proteins in early *Drosophila* embryos (Garcia De Las Bayonas et al., 2019). However, whether all three myosin pools in the SG are regulated by independent mechanisms or by a common module during epithelial tube formation remains unclear.

The contractile force of the actomyosin networks causes an increase of hydrostatic pressure in the cytoplasm (Charras et al., 2005). During epithelial morphogenesis, cells maintain the surface integrity by proper organization of actin at the cell cortex. Loss of organized cortical actin networks leads to the formation of blebs, spherical protrusions of the plasma membrane (Charras, 2008). During *Drosophila* gastrulation, blebs occasionally arise during apical constriction of mesodermal cells; these blebs correlate with apical F-actin holes (Costa et al., 1994; Jodoin et al., 2015). Disruption of cortical actin by latrunculin B, which sequesters globular actin (G-actin) and prevents filamentous actin (F-actin) assembly, enhances blebbing in epithelial cells in early *Drosophila* embryos (Kanesaki et al., 2013). Mutations in heterotrimeric G proteins also enhance blebbing (Kanesaki et al., 2013), suggesting a role of G proteins in stabilizing cortical actin. The mechanisms of cortical actin regulation during epithelial tube formation are not well understood.

Here, we reveal multiple roles of Smog GPCR in regulating actomyosin networks during *Drosophila* SG tube formation. We show that the GPCR Smog transduces Fog signal to regulate myosin contractility in the apicomedial region of SG cells to drive apical constriction during SG invagination. Our study supports a model wherein Smog regulates apicomedial and junctional/supracellular myosin pools in a Fog-dependent and -independent manner, respectively. We further reveal new roles of Smog in regulating the microtubule networks, key apical and junction proteins, and cortical actin organization during SG invagination, suggesting multifunctional roles of GPCR signaling during epithelial tube formation.

Results

Smog transduces Fog signal in the SG

To test the role of Smog in transducing Fog signal during SG invagination, we first examined *smog* transcripts and Smog protein levels in the developing SG. Consistent with the ubiquitous expression of *smog* (Kerridge et al., 2016), fluorescent in situ hybridization revealed low levels of *smog* mRNA expression in the entire embryo, including the SG. Strong *smog* mRNA signals were observed in SG cells near the invagination pit (Fig. 1B, B'), potentially due to the shrinking apical domain in those cells. We also examined Smog protein localization in the SG using a functional Smog-GFP fusion protein expressed under the control of the *sqh* promoter (Kerridge et al., 2016). Smog-GFP signals were detected as small punctate structures enriched near AJs in SG cells (Fig. 1C-C''). Importantly, Smog-GFP signals were dramatically increased in the entire apical domain of Fog-overexpressing SGs (Fig. 1D-D''; quantification in Fig. 1E), suggesting that Smog is recruited to the apical domain of SG cells by overproduced Fog.

To test whether Smog transduces Fog signal in the SG to regulate myosin contractility, we performed a genetic suppression test. We hypothesized that if Smog is a SG receptor for Fog, knocking down *smog* in the SG should suppress the gain-of-function effect of Fog. We used sqh-GFP, a GFP-tagged version of myosin regulatory light chain (Royou et al., 2004), and Rok-GFP, a GFP-tagged Rok fusion protein (Abreu-Blanco et al., 2014), as readouts of Fog signaling. sqh-GFP signals were significantly increased in the apicomedial region of Fog-overexpressing SG cells (compare Fig. 1G', G''' to Fig. 1F', F'''; quantification in Fig. 1H), suggesting increased myosin levels by Fog overexpression. Notably, sqh-GFP signals at AJs of SG cells were not significantly changed (Fig. 1I), suggesting that Fog promotes Rok accumulation and myosin activation in the apicomedial region of SG cells. Fog-overexpressing SG cells showed highly distorted AJs (Fig. 1G, G'') compared to control SG cells (Fig 1F, F''), suggesting increased pulling forces due to increased apicomedial myosin in Fog-overexpressing SG cells. Consistent with our finding that Fog signal promotes accumulation of Rok in the apicomedial region of SG cells (Chung et al., 2017), quantification of areas occupied by Rok-GFP puncta revealed overaccumulated Rok-GFP signals in the apicomedial

153 region of Fog-overexpressing SG cells (compare Fig. 1L', L''' to Fig. 1K', K'''; 154 quantification in Fig. 1N). Knockdown of *smog* in the SG using RNA interference (RNAi) 155 and the SG-specific *fkh-Gal4* driver (Henderson and Andrew, 2000) both suppressed 156 the apicomedial accumulation of Rok-GFP signals and reduced the magnitude of AJ 157 distortion (Fig. 1M-M'''; quantification in 1N, O). These data suggest that Smog 158 transduces Fog signal in the SG to facilitate Rok and myosin accumulation in the 159 apicomedial region of SG cells.
160
161 **Smog-transfected *Drosophila* S2 cells contract upon Fog signal**
162 To further test the role of Smog in transducing Fog signal to regulate myosin 163 contractility, we performed an in vitro cell contraction assay using *Drosophila* S2 cells. 164 S2 cells do not express Fog receptors, and therefore, do not respond to Fog in the 165 normal culture condition (Manning et al., 2013; Fig. 2A-B'). As shown in a previous 166 study (Manning et al., 2013), S2 cells transfected with Mist, the mesoderm-specific 167 receptor for Fog, contracted robustly when cultured in Fog-containing media (Fig. 2C- 168 D'). Since Smog was not detectable in *Drosophila* S2 cells (modENCODE Cell Line 169 Expression Data; Flybase), we tested if S2 cells transfected with Smog also contract 170 upon Fog treatment. Indeed, Smog-transfected cells showed a significantly higher 171 percentage of contraction upon Fog treatment compared to non-transfected S2 cells 172 (Fig. 2A-B', E-F'; quantification in Fig. 2G). Thus, Smog can transduce Fog signal to 173 regulate cellular contractility both in the SG and in vitro.
174
175 **Smog is required for apical constriction in the SG and epithelial morphogenesis 176 during embryogenesis**
177 To test the possibility that Smog functions as a Fog receptor in the SG, we knocked 178 down *smog* in the SG (using *fkh-Gal4*) using RNAi and compared apical areas of SG 179 cells to those in *fog* mutants. Two independent short hairpin RNAi lines, 180 *TRiP.HMC03192* (a stronger line; Fig. 3B, B'; also used for genetic suppression assay 181 in Fig. 1J-J''') and *TRiP.GL01473* (a weaker line; Fig. S1B, B'), were used. Cell 182 segmentation analysis revealed that SG cells with smaller apical areas showed a less 183 coordinated spatial distribution in *smog* RNAi SGs compared to control (Fig. 3A-B'; Fig.

184 S1B-C'), similar to the previously reported *fog* mutant phenotype (Chung et al., 2017;
185 Fig. S1A, A'). Quantification of percentage and cumulative percentage of cells of
186 different apical areas also revealed that SGs with *smog* knockdown with either RNA line
187 show larger apical areas compared to control (Fig. 3G; Fig. S1D), suggesting defective
188 apical constriction upon *smog* knockdown.
189 Since *smog* has a strong maternal contribution (Flybase Developmental RNA-Seq), we
190 also knocked down *smog* both maternally (using *matα-Gal4*; Häcker and Perrimon,
191 1998) and zygotically in the SG (using *fkh-Gal4*) and observed slightly more severe
192 apical constriction defects in SG cells (hereafter referred to as *smog* M/Z knockdown;
193 Fig. 3C, C'; quantification in 3G). Maternal knockdown of *smog* using the stronger RNAi
194 line (*TRiP.HMC03192*) resulted in severe defects in egg-laying. Therefore, all M/Z
195 knockdown experiments were performed using the weaker line (*TRiP.GL01473*).
196 Consistent with the ubiquitous expression of *smog* and its role in epithelial
197 morphogenesis in the early *Drosophila* embryo (Kerridge et al., 2016), *smog* M/Z
198 knockdown also resulted in a slight disruption of the overall embryonic morphology,
199 including defects in the head region, a wavy embryo surface, and an irregular ventral
200 midline (Fig. 3M, N). Unlike the circular SG placode of WT, *smog* M/Z knockdown also
201 resulted in a SG placode that was elongated along the dorsal/ventral axis (compare Fig.
202 3A, A' to 3C, C'). 3D reconstruction of confocal images revealed disrupted epithelial
203 morphology in *smog* M/Z knockdown, with wide and wavy grooves, enlarged epithelial
204 cells, and an elongated SG placode (Fig. 3I, J).
205 *smog* zygotic null mutants had a range of defects similar to those observed with *smog*
206 RNAi knockdown (Kerridge et al., 2016). 73.8% of embryos (59/80) showed relatively
207 normal embryonic morphology with mild apical constriction defects in SG cells, like
208 *smog* zygotic knockdown (classified as '*smog* null [mild]'; Fig. 3D-E', K; quantification in
209 3H); 26.2% of embryos (21/80) showed a disrupted embryonic morphology with SGs
210 elongated along the dorsal/ventral axis (Fig. 3F, F', L) and more severe apical
211 constriction defects (Fig. 3H), like *smog* M/Z knockdown (classified as '*smog* null
212 [severe]'). All embryos at late stages (stages 15-17) *smog* null mutants showed
213 relatively normal embryonic morphology (Fig. S2A, B), suggesting that severely
214 defective embryos with *smog* loss do not survive/develop past stage 14. Notably, these

215 embryos have relatively normal internalized SGs (Fig. S2F, G), except for rare cases of
216 crooked SG morphology (Fig. S2D), confirming our previous finding that apical
217 constriction is not required for SG internalization (Chung et al., 2017). Altogether, these
218 data suggest that Smog is required for coordinated apical constriction during SG
219 invagination and proper epithelial morphogenesis during embryogenesis.
220

221 **Smog regulates apicomedial and junctional myosin in a Fog-dependent and -**
222 **independent manner in the SG**

223 We next examined myosin levels and distribution in the SGs in *smog* knockdown or
224 *smog* mutants using sqh-GFP. Apicomedial myosin, which generates the pulling force
225 for apical constriction during SG invagination (Booth et al., 2014), is the only myosin
226 pool defective in the SGs of *fog* mutants (Chung et al., 2017). Consistent with the idea
227 that Smog transduces Fog signal in the SG, both *smog* knockdown (either zygotic or
228 M/Z knockdown) and *smog* loss resulted in a significant reduction in the intensity of
229 apicomedial myosin in SG cells near the invagination pit, compared to control (Fig. 4 A-
230 D''; quantification in 4I). Moreover, compared to clear web-like structures of apicomedial
231 myosin in control SG cells (Fig. 4A-A''), SG cells in *smog* knockdown or *smog* null
232 mutants showed reduced areas of sqh-GFP puncta, suggesting dispersed myosin along
233 the entire apical surface in SG cells (Fig. 4K). Interestingly, the intensity of junctional
234 myosin was also significantly reduced in SG cells with *smog* knockdown or *smog* loss,
235 compared to control (Fig. 4A-D'', quantification in 4J). This phenotype is distinct from
236 what was observed in *fog* mutants, where junctional myosin was unaffected in SG cells
237 (Chung et al., 2017). We conclude that Smog is required for maintaining normal levels
238 of both apicomedial and junctional myosin in the SG in a Fog-dependent and -
239 independent manner, respectively.

240 We also tested Rok distribution in SG cells in *smog* RNAi and *smog* null mutants, using
241 Rok-GFP. Consistent with our previous study (Chung et al., 2017), Rok-GFP formed
242 large punctate structures in the apicomedial region in control SG cells (Fig. 4E-E'').
243 However, Rok-GFP failed to accumulate and was dispersed along the entire apical
244 domain in SG cells in *smog* knockdown and *smog* null mutants (Fig. 4F-H'';
245 quantification in 4L), similar to the dispersed Rok-GFP distribution observed in *fog*

246 mutant SG cells (Chung et al., 2017). These data suggest that Smog is required for Rok
247 accumulation in the apical domain of SG cells.

248

249 ***smog* loss leads to defects in the tissue-level myosin cable**

250 Reduced myosin levels and the elongated SG placode in *smog* null [severe] embryos
251 led us to test the third pool of myosin in the SG, the supracellular myosin cable
252 surrounding the SG placode. Consistent with the idea that this myosin cable is under
253 tension (Chung et al., 2017; Röper, 2012), WT SGs showed a relatively smooth tissue
254 boundary (Fig. 4M-M''). However, SGs in *smog* null [severe] embryos showed an
255 irregular boundary and a less clear myosin cable (Fig. 4N-N''). We calculated the
256 circularity of the SG placode as a measure of smoothness and tension of the SG
257 boundary. The circularity of the WT placode was significantly higher than the circularity
258 of one cell row inside (inner boundary) or outside of SG placode (outer boundary),
259 suggesting a higher tension of the myosin cable in WT (Fig. 4O, P). Consistent with the
260 irregular SG boundary in *smog* null [severe], the circularity of the SG placode in *smog*
261 null embryos was significantly lower than that of WT and was not statistically significant
262 from the inner or outer boundaries, suggesting a lack of tension at SG boundary in
263 *smog* null mutants (Fig. 4P). Overall, our data suggest that the loss of *smog* affects all
264 myosin pools in the SG, including the myosin at the SG boundary, leading to reduced
265 tension at the SG boundary and defects in generating the compressing force.

266

267 **Smog is required for proper localization of apical and junctional components and**
268 **microtubule networks in epithelial cells**

269 Since we observed a range of defects in whole embryo morphology in *smog* mutants,
270 we explored the potential cellular basis. In stage 11 *smog* null [severe] embryos, we
271 occasionally observed large areas in the epidermis and the SG where E-Cad (Fig. 5B,
272 B') and Crb (Fig. 5D, D') signals were absent or significantly reduced. Similar defects
273 were observed in late-stage (stage 14) embryos. Crb levels were significantly reduced

274 in large areas; in the most severe cases, Crb was dispersed in the entire epidermis (Fig.
275 S3B, B'). These data suggest that Smog is required for maintaining epithelial polarity
276 and junctional integrity by regulating E-Cad and Crb levels or distribution.
277 To better understand the basis of the reduced E-Cad and Crb in *smog* mutants, we
278 examined *smog* null mutant SG cells at higher magnification. Even SGs that do not
279 contain large patches where E-Cad/Crb are missing showed discontinuous E-Cad/Crb
280 signals, resulting in small gaps in signal along the SG cell boundary (Fig. 5F, G, I, J).
281 Such gaps were observed in both *smog* null [mild] and *smog* null [severe] embryos.
282 Although the number and the length of gaps in E-Cad signals in *smog* null [mild] were
283 comparable to those of WT, they were significantly higher in *smog* null [severe]
284 compared to WT (Fig. 5F, G; quantification in 5K, L). The number and the length of
285 gaps in Crb signals in SG cells were significantly higher in both mild and severe *smog*
286 null mutant embryos compared to WT (Fig. 5I, J; quantification in 5M, N). These data
287 suggest a role of Smog in regulating Crb and E-Cad levels and continuity during
288 epithelial morphogenesis, including the SG.

289 Anisotropic localization of Crb at the SG boundary has been suggested to drive the
290 formation of supracellular myosin cable in SG (Röper, 2012). Consistent with this, in
291 control SGs, Crb levels were higher in the junctions that did not contribute to the myosin
292 cable, whereas myosin was highly enriched at the junction forming the cable at the SG
293 boundary (Fig. S3C-E'''). However, in several *smog* null [severe] SGs, the overall Crb
294 intensity was quite low, and Crb did not show an anisotropic localization at the SG
295 boundary (Fig. S3F-H''). This data suggests that *smog* loss results in the reduction of
296 both myosin and Crb, failing to form the supracellular myosin cable at the SG boundary.

297 Microtubules are required for forming and maintaining apical myosin structures (Booth
298 et al., 2014; Ko et al., 2019) and for transporting several key apical and junctional
299 proteins in *Drosophila* tubular organs, including E-Cad and Crb (Le and Chung, 2021; le
300 Droguen et al., 2015). We recently showed that microtubule-dependent intracellular
301 trafficking has an important role in regulating apical constriction and apicomedial myosin
302 during SG invagination (Le and Chung, 2021). To examine the microtubule networks in
303 the SG of wild-type and *smog* mutant embryos, we stained with antibodies against

304 acetylated-α-tubulin, a marker of stable, long-lived microtubules, and tyrosinated-α-
305 tubulin, a marker of dynamic, short-lived microtubules (Westermann and Weber, 2003).
306 We observed a reduction of both acetylated-α-tubulin and tyrosinated-α-tubulin signals
307 in the apical region of the SG in *smog* mutants, compared to wild type (compare Fig.
308 5O, Q to Fig. 5P, R; quantification in 5S), suggesting disrupted microtubule networks in
309 the SG in *smog* mutants. This finding suggests that loss of *smog* could affect apical
310 pools of myosin, Crb and E-Cad through effects on microtubule abundance, distribution
311 and/or polarity.

312

313 **Smog is required for cortical actin organization in the SG**

314 We observed numerous blebs in the apical membrane of SG cells in *smog* null [severe]
315 mutants, which were most prominent near the invagination pit (compare Fig. 6A-A''' to
316 Fig. 6B-B'''). Such blebs were not observed in SGs in WT, *smog* null [mild], or *fog*
317 mutant embryos (Fig. S4A-C''). Unlike dispersed Rok-GFP signals in *smog* knockdown
318 or *smog* null [mild] embryos (Fig. 4F-H''), Rok-GFP was enriched in many of these blebs
319 (Fig. 6B-B'''), consistent with Rok's recruitment to retracting blebs (Aoki et al., 2016). In
320 *smog* null [severe] embryos, blebs were also occasionally observed in cells outside the
321 SG placode (Fig. S4D-E''). During *Drosophila* gastrulation, bleb formation correlates
322 with cortical F-actin holes (Jodoin et al., 2015), and disruption of cortical actin enhances
323 blebbing (Kanesaki et al., 2013). We therefore tested if Smog affects the cortical actin
324 network during apical constriction in the SG. Indeed, phalloidin staining revealed that
325 whereas strong F-actin signals were observed in the apical domain of SG cells near the
326 invagination pit in WT, F-actin was significantly reduced in SGs in *smog* mutants (Fig.
327 6C-C', 6D-D').

328 Apical F-actin formation in *Drosophila* tubular organs requires the formin family actin
329 nucleator Diaphanous (Dia) (Massarwa et al., 2009; Rousso et al., 2013). Since the
330 apical localization and activity of Dia are critical for restricting F-actin formation to the
331 correct membrane domain, we tested the localization and levels of Dia in the SG in
332 *smog* mutants. Similar to reduced F-actin, we observed reduced Dia signals in the

333 apical domain of SG cells, most prominently near the invagination pit in *smog* mutants,
334 compared to WT (Fig. 6C-C'', D-D''). Quantification of the Dia intensity revealed that Dia
335 signals are reduced in the apicomedial but not in the junctional region of SG cells (Fig.
336 6E-G). Our data suggest that Smog is required for the cortical actin networks during SG
337 invagination, at least in part via modulating Dia levels.

338 We next tested if the reduction in actin levels in *smog* mutants is due to defects in actin
339 turnover. To test this, we modulated the level of actin regulators in the SG in *smog*
340 mutants and assayed the blebbing phenotype. Using RNAi, we knocked down
341 *chickadee* (*chic*), which encodes *Drosophila* profilin, a protein that increases F-actin by
342 promoting actin polymerization (Cooley et al., 1992), in the *smog* mutant background. If
343 there is a shift from F-actin to monomeric G-actin in *smog* mutants, we expect
344 enhancement of the disorganized actin phenotype and bleb formation with a reduced
345 *chic* level. Blebs were not observed in *smog* null [mild] embryos or in SGs knocked
346 down for *chic* in the otherwise wild-type background (Fig. 6H-H''; Fig. S4B-B'').
347 However, when *chic* was knocked down in the SG in the *smog* mutant background, we
348 observed enhanced blebbing even in mildly defective SG cells (Fig. 6I-I''). Since profilin
349 promotes formin-mediated actin filament assembly (Romero et al., 2004; Zweifel and
350 Courtemanche, 2020), our data suggests that reduced profilin by *chic* knockdown
351 aggravated defects in cortical actin organization with reduced Dia in *smog* mutants.
352 Overall, our data suggest that Smog is required for cortical actin organization as well as
353 myosin activation during epithelial morphogenesis.

354

355 **Discussion**

356 **Smog regulates different pools of myosin in a Fog-dependent and -independent**
357 **manner during SG invagination**

358 Fog signaling triggers epithelial cell shape changes driving tissue folding and
359 invagination during development of *Drosophila* and other insects (Benton et al., 2019;
360 Manning and Rogers, 2014). During *Drosophila* embryogenesis, *fog* is upregulated in
361 multiple tissues undergoing apical constriction and tissue invagination, such as ventral
362 furrow (mesoderm), the posterior midgut (endoderm), and the SG (ectodermal
363 derivative) (Nikolaidou and Barrett, 2004). During *Drosophila* gastrulation, the
364 ubiquitously expressed GPCR Smog and the mesoderm-specific GPCR Mist respond to
365 Fog signal to regulate myosin contractility during mesoderm invagination (Kerridge et
366 al., 2016; Manning et al., 2013). Here, we provide evidence that Smog functions as a
367 SG receptor for Fog to activate myosin during SG invagination. Knockdown of *smog* by
368 RNAi suppresses the gain-of-function effect of Fog in the SG (Fig. 1). Also, Smog-
369 transfected S2 cells contract upon Fog signal (Fig. 2), suggesting that Smog responds
370 to Fog to regulate myosin contractility both in vivo and in vitro. Our data show that Fog
371 overexpression leads to Smog recruitment to the apicomedial region of SG cells (Fig.
372 1). Consistent with our data, Fog overexpression induces oligomerization of Smog in
373 early *Drosophila* embryos (Jha et al., 2018).

374 Our study also dissects the roles of Smog in myosin activation during SG
375 morphogenesis and reveals Fog-independent roles of Smog. Whereas *fog* mutants
376 exhibit a decrease in only the apicomedial myosin pool in SG cells (Chung et al., 2017),
377 *smog* loss and SG-specific knockdown of *smog* result in a significant reduction of both
378 apicomedial and junctional myosin (Fig. 4). We propose that Smog regulates junctional
379 myosin during epithelial morphogenesis in response to an unknown, ubiquitously
380 expressed ligand and regulates apicomedial myosin in response to Fog in tissues with
381 high Fog signals, such as the mesoderm (Kerridge et al., 2016; Manning et al., 2013)
382 and the SG (this study). Consistent with this model, during *Drosophila* gastrulation,
383 Smog activates different myosin pools in tissues with different Fog levels. In the
384 mesoderm, where Fog levels are high, Smog and Mist transduce Fog signal to activate

385 myosin in the apicomedial region and drive apical constriction. In the ectoderm, where
386 Fog levels are very low, Smog is required for junctional myosin activation to drive cell
387 intercalation. SG cells undergo both apical constriction and cell intercalation, and our
388 data shows that Smog regulates both pools of myosin in the SG in a Fog-dependent
389 and -independent manner. It is possible that in tissues with high Fog signals, an
390 additional tissue-specific GPCR(s) function with Smog in response to Fog to fine-tune
391 the Fog signaling for proper apical constriction, like Mist does in the mesoderm. It will be
392 interesting to determine whether additional SG-specific GPCRs function with Smog
393 during SG invagination.

394 The downstream components that transduce signals from the Smog GPCR to regulate
395 myosin in distinct regions of SG cells await discovery. Good candidates include two Rho
396 guanine nucleotide exchange factors (RhoGEFs), RhoGEF2 and Dp114RhoGEF, which
397 have been shown to activate Rho1 signaling at the apicomedial and junctional domain
398 of epithelial cells, respectively (Garcia De Las Bayonas et al., 2019). This process
399 requires upstream activation by heterotrimeric G proteins $G\alpha_{12/13}$/Cta and Gβ13F/Gγ1 at
400 the apicomedial and junctional domains, respectively (Garcia De Las Bayonas et al.,
401 2019). Thus, distinct ligand-receptor binding with Smog may activate distinct G proteins
402 and/or RhoGEFs in the apicomedial and junctional domains.

403

404 **Smog regulates cortical actin organization during SG invagination independent of**
405 **Fog**

406 We also discover that Smog regulates cortical F-actin organization during SG
407 invagination (Fig. 6). *smog* loss significantly reduces levels of F-actin and the formin
408 protein Dia (Fig. 6). Rho1 regulates actin polymerization via Dia (Goode and Eck, 2007),
409 and apical F-actin formation in the *Drosophila* SG requires apical localization and
410 activity of Dia (Massarwa et al., 2009; Rousso et al., 2013). Our data suggest that Smog
411 activates Rho1 signaling to regulate both cortical F-actin (via Dia) and myosin (via Rok)
412 (Fig. 7). Since mutations in *fog* do not enhance blebbing during SG invagination (Fig.
413 S4), Smog's role in regulating cortical actin is independent of Fog. Supporting our data,

414 during *Drosophila* gastrulation, *fog* mutants show normal GFP-Moesin signals in the
415 ventral furrow, suggesting normal cortical actin organization upon *fog* loss (Kanesaki et
416 al., 2013). $G\alpha_{12/13}$/Cta is a key component downstream of Fog that recruits RhoGEF2 to
417 the apical membrane to regulate myosin contractility (Barrett et al., 1997; Dawes-Hoang
418 et al., 2005). Interestingly, mutations in Gαi (G-iα65A) and Gβ13F/Gγ1, but not
419 $G\alpha_{12/13}$/Cta, disrupt cortical actin organization in early *Drosophila* embryos (Fox and
420 Peifer, 2007; Kanesaki et al., 2013). Therefore, Smog may signal through Gαi and/or
421 Gβ13F/Gγ1 to organize cortical actin, independent of Fog and $G\alpha_{12/13}$/Cta.

422 The link between heteromeric G proteins and Rho1 signaling occurs through activation
423 of specific RhoGEFs (Vázquez-Victorio et al., 2016). Actin polymerization resulting from
424 Fog-independent Smog activation may imply the recruitment of distinct proteins
425 modulating the activation of Rho1-mediated pathways. For example, in the absence of
426 Fog, a specific RhoGEF(s) downstream of Gαi or Gβ13F/Gγ1 may link Smog and Rho1
427 signaling to regulate cortical actin organization; upon high Fog signals, a different Rho1
428 modulator(s) downstream of $G\alpha_{12/13}$/Cta may be recruited to facilitate apicomedial
429 myosin formation. Further work is needed to identify the link between Smog and Rho1
430 activation in the presence or absence of Fog during SG invagination. It will be also
431 interesting to determine whether Fog-independent roles of Smog–regulating cortical
432 actin and junctional myosin–involve common or distinct Rho1 modulators.

433

434 **Smog regulates epithelial integrity during development**

435 *smog* null mutant embryos show a range of defects, allowing us to dissect the roles of
436 Smog in epithelial morphogenesis. Our data reveal that Smog is required for epithelial
437 integrity by affecting levels and localization of Crb and E-Cad (Fig. 5). Since the
438 decrease in the level of Crb and E-Cad in *smog* mutants correlates with significantly
439 reduced myosin levels, disrupted epithelial integrity may be due to disrupted actomyosin
440 networks. Myosin II is critical for cells to concentrate E-cadherin at cell-cell contacts
441 (Shewan et al., 2005). In early *Drosophila* embryos, the absence of contractile myosin
442 leads to the disassembly of junctions (Weng and Wieschaus, 2016). A possible scenario

443 is that Smog is required to recruit key Rho1 regulators, such as RhoGEF2,
444 Dp114RhoGEF, or other SG-upregulated RhoGEFs, to AJs during SG invagination to
445 promote junctional myosin assembly. Since Dia helps coordinate adhesion and
446 contractility of actomyosin (Homem and Peifer, 2008) and formin-mediated actin
447 polymerization at AJs stabilizes E-Cad and maintains epithelial integrity (Rao and
448 Zaidel-Bar, 2016), reduced Dia levels in *smog* mutants may also contribute to loss of
449 epithelial integrity.

450 Reduced and discontinuous signals of apical and junctional components in *smog*
451 mutant embryos can also be due, in part, to compromised intracellular trafficking.
452 Disorganized microtubule networks in SGs in *smog* mutants (Fig. 5) support this idea.
453 Our recent study showed that microtubule- and Rab11-dependent intracellular
454 trafficking regulates apical myosin pools and apical constriction during SG invagination,
455 via apical enrichment of Fog and the continuous distribution of Crb and E-Cad along
456 junctions (Le and Chung, 2021). The mechanism of how Smog affects microtubule
457 organization remains to be revealed. Overall, our findings suggest the multifaceted roles
458 of Smog during epithelial tube formation in regulating distinct myosin pools and cortical
459 actin in different subcellular domains in a ligand-dependent manner.

460

461

462 **Materials and Methods**

463 **Fly stocks and genetics**

464 The fly stocks used in this study are listed in Table S1. All the crosses were performed
465 at 25°C.

466

467 **Immunofluorescence and confocal microscopy**

468 *Drosophila* embryos were collected on grape juice agar plates supplemented with yeast
469 paste at 25℃. Embryos were dechorionated with 50% bleach. For most samples,
470 embryos were fixed in 1:1 heptane: formaldehyde for 40 minutes and devitellinized with
471 80% EtOH. For Rok-GFP, Sqh-GFP, and phalloidin staining, embryos were hand-
472 devitellinized. Embryos were then stained with primary and secondary antibodies in
473 PBSTB (1X PBS with 0.1% Triton X-100 and 0.2% bovine serum albumin) and PBTr
474 (1X PBS with 0.1% Triton X-100) for EtOH devitalization and hand-devitalization,
475 respectively. Antibodies used in our experiments are listed in Table S2. Embryos were
476 mounted in Aqua-Poly/Mount (Polysciences, Inc) and imaged with a Leica TCS SP8
477 confocal microscope using 63x, NA 1.4 and 40x, NA 1.3 objectives. Images were
478 acquired as z-stacks (each 0.3 μm apart) that span the apical and junctional domains of
479 cells in the SG placode.

480

481 **Fluorescent in situ hybridization**

482 Embryos were fixed using formaldehyde/heptane for 30 min followed by devitellinization
483 with methanol. SP6 polymerase-synthesized digoxigenin (DIG)-labeled antisense probe
484 was prepared using the following primers: *smog*-F, 5'-ACAGAGCCCACCTGTGTAGG-
485 3'; *smog*-R, 5'-TCGCTGATCGAAAATGATCTC-3'. Fluorescent in situ hybridization was
486 performed using standard methods as described in (Knirr et al., 1999). Briefly, the
487 embryos were pre-hybridized for 1 hour at 56°C post-fixation. Following this step, the
488 embryos were hybridized with the probe overnight at 56°C. The next day, embryos were
489 stained for DIG using the anti-DIG primary antibody and biotin-conjugated secondary
490 antibody. The embryos were then incubated with AB solution (PK-6100, VECTASTAIN
491 Elite ABC kit). Tyramide signal amplification reaction was performed using Cy3
492 fluorescent dye (diluted 1:50 using amplification diluent) (Perkin Elmer Life Sciences,

493 Inc., NEL753001kt). The embryos were co-stained with CrebA and Crb antibodies for
494 visualizing SG nuclei and apical cell boundaries, respectively.

495

496 **Total Smog-GFP intensity**

497 Maximum intensity projections of two z-sections that span the apical and the junctional
498 region of SG cells were used. Intensity means of Smog-GFP signals of SG cells in the
499 entire SG placode were measured using Imaris software. The mean intensity of Smog-
500 GFP was normalized by the median deviation. The integrated density of Smog-GFP
501 was calculated by multiplying the apical area of the cell with the mean intensity of each
502 cell. Total Smog-GFP signals within the whole placode were calculated as the sum of
503 the integrated density of all cells. For background correction, mean gray values of
504 Smog-GFP in ten cells outside of the SG placode were measured. The average value of
505 mean gray values of Smog-GFP in these ten cells was used to subtract the background
506 of the cells inside the placode from the same embryo. Four and five SGs were used to
507 quantify control and Fog overexpression, respectively. P values were calculated using
508 Welch's t-test in the GraphPad Prism software.

509

510 **Cell segmentation and apical area quantification**

511 SGs that were invaginated within the range of 4.8-9.9 μm depth were used for
512 quantification. Two or three z-sections of the apical domain were used to generate a
513 maximum intensity projection (Leica LasX software). SG cells were marked using CrebA
514 and segmented along E-Cad signals using the Imaris program. Apical areas of
515 segmented cells were calculated using Imaris, and cells were color-coded based on
516 their apical domain size. Frequency distribution was performed using GraphPad Prism.
517 Apical areas from eight SGs were quantified in control, *smog* knockdown (Z), and *smog*
518 null [mild] embryos. Six SGs were used for quantification for *smog* knockdown (M/Z)
519 and *smog* null [severe] embryos. Statistical significance was determined using Mann-
520 Whitney U test (percentage of cells) and Kolmogorov-Smirnov test (cumulative
521 percentage of cells).

522

523 **Quantification of myosin and Dia intensity in the apicomedial and junctional**
524 **domains**
525 Maximum intensity projection of two z-sections spanning apical and junctional regions of
526 SG cells with Sqh-GFP and E-Cad signals was used. The images were then exported to
527 ImageJ and converted to RGB stack image type. Twenty cells near the invagination pit
528 in each of five SGs were used for quantification. To calculate the apicomedial and
529 junctional myosin intensity, regions were drawn manually along the inner and outer
530 boundary of the E-Cad signal of each cell, and mean gray values were measured for
531 apicomedial and junctional myosin. For background subtraction, the average mean gray
532 value of sqh-GFP signals for ten cells outside the SG placode was subtracted from the
533 mean gray value of apicomedial and junctional myosin for each SG cell. SuperPlots
534 (Lord et al., 2020) were used to address the variability of datasets in each SG. Each
535 data point in the graph represents one SG consisting of twenty cells used for
536 quantification. Statistical significance was determined using Welch's t-test. Dia intensity
537 in the apicomedial and junctional domain of SG cells was quantified using the same
538 strategy, with ten cells near the invagination pit in each of five SGs.
539
540 **Quantification of areas of Rok-GFP and apicomedial myosin particles**
541 A single z-section of the confocal image with the strongest Rok-GFP signals in the
542 apicomedial region was used. Rok-GFP signals were converted to black and white
543 using the threshold tool in Adobe Photoshop. Junctional Rok-GFP signals were
544 removed manually based on E-Cad signals. Areas of Rok-GFP puncta were determined
545 using the Analyze Particles tool in ImageJ. Rok-GFP puncta with area ≥0.02 μm^2 was
546 measured. Fifteen cells in the dorsal posterior region near the invagination pit of the SG
547 placode were used for quantification. The same strategy was used for Sqh-GFP signals
548 to quantify the area of apicomedial myosin. SuperPlots show mean values of data
549 points of five SGs. Statistical significance was determined using Welch's t-test.
550
551 **Quantification of the waviness of junctions**
552 Using a single z-section with the highest E-Cad signals and ImageJ software, the
553 shortest (L_0) and the actual distance (L) between vertices were measured in SG cells.

554 The ratio of these distances (L/L_0) was used as the waviness of junctions. 10-15 cells
555 near the invagination pit in each of five SGs were used for quantification. Statistical
556 significance was determined using Welch's t-test.
557
558 **Quantification of number and length of gaps of Crb and E-Cad**
559 The number and the length of gaps for Crb and E-Cad signals were measured using
560 confocal images and ImageJ. A single z-section with the highest Crb or E-Cad signals
561 was chosen for quantification. Gaps with a length ≥0.2 μm were used for quantification.
562 All junctions from ten cells in five SGs were quantified. If there were multiple gaps on a
563 junction, we added the length of all the gaps on that junction to calculate the ratio of the
564 length of gaps to junctional length. Statistical significance was determined using
565 Welch's t-test.
566
567 **Circularity of the SG boundary**
568 Using confocal images and ImageJ, cell boundaries were manually drawn along E-Cad
569 signals at the SG placode boundary and one cell row outside and inside the placode.
570 For most samples, strong myosin cable signals at the dorsal, anterior, and posterior
571 boundaries of the placode and CrebA signals in SG cells were used to determine the
572 SG boundary. In *smog* null [severe], where myosin signals were significantly reduced in
573 all cells, CrebA signals were used to determine the boundary. The ventral midline was
574 used as the ventral boundary of the SG in all cases. The perimeter and the area of the
575 SG corresponding to these boundaries were measured using ImageJ, and circularity
576 was calculated using the formula, $C = 4\pi \text{ area}/\text{perimeter}^2$. For a perfect circle, the value
577 of circularity should be 1. Five SGs were used for quantification, and statistical
578 significance was determined using Welch's t-test.
579
580 **Tyrosinated tubulin intensity quantification**
581 Three z sections spanning the most apical region of SG cells were used for
582 quantification. The mean intensity of tyrosinated tubulin signals in the whole SG placode
583 was measured using ImageJ. The area of the SG was drawn manually based on the E-
584 Cad and CrebA signals to label the cell boundary and SG nuclei, respectively. For

585 background correction, the mean intensity of ten cells outside the SG of the same
586 embryo was used. The ratio of the mean intensity of tyrosinated tubulin signals inside
587 the placode to the mean intensity of control cells outside the placode was calculated
588 and plotted. Four and five SGs were used for control and *smog* mutant, respectively. t-
589 test with Welch's correction was used to calculate the p value.
590
591 **Cell contractility assay**
592 cDNA clones for *smog* (RE70685) and *mist* (RE13854) were obtained from *Drosophila*
593 Genomics Resource Center (DGRC). Isolated cDNAs were cloned into the pMT-V5-
594 HisB vector (Addgene) using the conventional restriction digestion and ligation method.
595 Primers with restriction sites used to isolate the open reading frame are stated below
596 (restriction sites underlined).
597
598 *smog* CDS-EcoRI-5', 5'-CCGGAATTCATGGAACTGTGCATAGCAAC-3'
599 *smog* CDS-NotI-3', 5'-ATTTGCGGCCGCATTGGTCGTGATTGTATCTTTGG-3'
600 *mist* CDS-EcoRI-5', 5'-CCGGAATTCATGGACAGGAGTCGGAGTAGC-3'
601 *mist* CDS-NotI-3', 5'-ATTTGCGGCCGCAGCAAATGGTCTCCATTTTG-3'
602
603 S2 and S2-Mt-Fog-myc cells (Manning et al., 2013) were obtained from DGRC. Shields
604 and Sang M3 insect media (HiMedia) was used with 10% Fetal Bovine Serum (Corning)
605 and 1:1000 Antibiotic-Antimycotic (Gibco). Cells were cultivated at 25°C either in 25-cm^2
606 flask in 5 ml media or 75-cm^2 flask in 15 ml media. To prepare for the Fog media, S2-
607 Mt-Fog-myc cells were grown undisturbed for 4-8 days to attain approximately 100%
608 confluency. 50 µl of 100 mM CuSO4 was added to nearly 100% confluent cells in 75-
609 cm^2 flask to induce metallothionein promoter. The Fog-containing media was collected
610 by centrifugation and further concentrated using 3,000 MW concentrators. The
611 presence of Fog was confirmed by Western blot using the Myc-antibody (Invitrogen;
612 RRID:AB_2533008). Non-transfected S2 cells were used as a control.
613 Cell contractility assay was performed as described in (Manning et al., 2013). Smog- or
614 Mist-transfected S2 cells were induced with $CuSO_4$. Cells were then transferred to
615 Concanavalin A-coated coverslips and fixed using 10% paraformaldehyde in PBTr for

616 15 minutes at room temperature (RT). After being blocked in 5% NGS in PBTr for 20
617 minutes at RT, cells were stained with the V5 antibody (Invitrogen; RRID:AB_2556564)
618 to differentiate between transfected and non-transfected cells. Cell contractility of
619 transfected cells was monitored using a phase-contrast filter in a Leica DM2500
620 microscope using the 40X, 0.8 NA objective. Two-way ANOVA was performed to
621 calculate statistical significance.
622
623 **Fly strains used (Table S1)**

Fly strain	**Sources and References**	**RRID**
Oregon R (wild type)		
fkh-Gal4	Henderson and Andrew, 2000	BDSC_78060
matα4-Gal4 (on II)	Bloomington Stock Center	BDSC_7062
matα4-Gal4 (on III)	Bloomington Stock Center	BDSC_7063
UAS-Fog	Dawes-Hoang et al., 2005	
smog-GFP	Kerridge et al., 2016	
ubi-Rok-GFP	Abreu-Blanco et al., 2014	BDSC_52289
sqh-GFP	Royou et al., 2004	BDSC_57144
sqh-mCherry	Martin et al., 2009	BDSC_59024
smog null mutant	Kerridge et al., 2016	
fog^{RA67}		BDSC_6218
UAS-Dicer-2	Vienna *Drosophila* Resource (#60008)	
TRiP.GL01473 (*smog* RNAi (weak))	Bloomington Stock Center	BDSC_43135
TRiP.HMC03192 (*smog* RNAi (strong))	Bloomington Stock Center	BDSC_51705

TRiP.HMS00550 (*chic* RNAi)	Bloomington Stock Center	BDSC_34523

624

625 **Antibodies Used (Table S2)**

626

Antibody	Source	RRID	Dilution
α-E-Cad (rat)	DSHB (DCAD2)	AB_528120	1:50
α-CrebA (rat)	Andrew lab (John Hopkins University); This study		1:3000
α-CrebA (rabbit)	Andrew lab (John Hopkins University)	AB_10805295	1:5000
α-GFP (chicken)	Invitrogen (A10262)	AB_2534023	1:500
α-β-galactosidase (rabbit)	Invitrogen (A11132)	AB_221539	1:500
α-β-galactosidase (mouse)	Invitrogen (MA5-15222)	AB_10980770	1:500
α-Crb (mouse)	DSHB (Cq4)	AB_528181	1:10
α-mCherry (rat)	Invitrogen (M11217)	AB_2536611	1:1000
α-Myc (mouse)	Invitrogen (13-2500)	AB_2533008	1:250
α-V5 (mouse)	Invitrogen (R960-25)	AB_2556564	1:400
α-Dia (rabbit)	Afshar et al., 2000		1: 5000
Phalloidin Alexa 488	Invitrogen (A12379)		1:250
Alexa Fluor 488/568/647-	Invitrogen		1:500

coupled secondary antibodies			

627

Acknowledgments

We thank the members of the Chung laboratory for comments and suggestions. We thank A. Martin, T. Lecuit and the Bloomington stock center for fly stocks, and D. J. Andrew and the Developmental Studies Hybridoma Bank for antibodies. We thank Flybase for the gene information. We are grateful to D. J. Andrew, C. D. Hanlon, J. Kim, and J. Matthew for their helpful comments on the manuscript. This work is supported by start-up fund from Louisiana State University and the grant from the Board of Regents Research Competitiveness Subprogram GR-00005224 to S.C.

637 **Figure Legends**

638 **Figure 1. Smog transduces Fog signal to activate Rok and myosin in the SG.** (A)
639 Cartoon diagram showing SG placodes (magenta) in the ventral side of a stage 11
640 *Drosophila* embryo. Cells that undergo apical constriction anterior to the invagination pit
641 (asterisk) are shown in purple. In those cells, the Fog ligand (yellow) binds to its GPCR
642 (blue) to activate apicomedial myosin. In all stage 11 SG images, anterior is to the left,
643 and dorsal is up. (B, B') Fluorescent in situ hybridization of *smog* (magenta) in the
644 invaginating WT SG. Strong *smog* mRNA signals are shown in apically constricting SG
645 cells near the invagination pit (arrowheads). CrebA (green), SG nuclei. White lines, SG
646 boundary. Arrows, *smog* signals near the grooves and the ventral midline. (C-D'')
647 Smog-GFP (green) signals in control (C-C'') and Fog-overexpressing SGs (D-D'').
648 Magenta, E-Cad. Control SG cells show puncta of Smog-GFP signals in the apical
649 region near AJs (yellow arrowheads). Considerably higher Smog-GFP signals in the
650 entire apical domain of Fog-overexpressing SG cells (red arrowheads). Insets,
651 magnified images of yellow boxed regions. (C'', D'') Z sections across the yellow lines in
652 C and D. (E) Quantification of total Smog-GFP intensity in control and Fog
653 overexpressing SG cells. n= 4 SGs (control); 5 SG (Fog overexpression). *p≤0.05
654 (Welch's t-test). (F, G) sqh-GFP (green) and E-Cad (magenta) signals in control (F) and
655 Fog-overexpressing (G) SGs. (F'-G''') Magnified images of yellow boxed regions in F
656 and G. Compared to control (F-F'''), sqh-GFP signals are increased in the apicomedial
657 region of Fog-overexpressing SG cells (G-G'''). Yellow arrowheads, AJs. Cyan
658 arrowheads, sqh-GFP signals. (H-J) Quantification of apicomedial myosin intensity (H),
659 junctional myosin intensity (I), and the ratio of apicomedial to junctional myosin intensity
660 (J). (K-M''') Rok-GFP (green) and E-Cad (magenta) signals in SGs. K'-M''', magnified
661 images of yellow boxed regions in K-M. Compared to control (K-K'''), Fog-
662 overexpressing SG shows overaccumulation of Rok-GFP and wavy cell junctions (L-
663 L'''). *smog* knockdown suppresses these phenotypes (M-M'''). Yellow arrowheads, AJs.
664 Cyan arrowheads, Rok-GFP puncta. (N, O) Quantification of the area of Rok-GFP
665 particles (N) and waviness of AJs (O). Asterisks, invagination pit. n=5 SGs, 75 cells for
666 each genotype in H-J, N, and O. *p≤0.05; **p≤0.01; ***p≤0.001; ****p≤0.0001 (Welch's t-
667 test).

668

669 **Figure 2. Smog-transfected S2 cells contract in response to Fog. (**A-F') S2 cells
670 cultured in the absence (A, C, E) or presence (B, D, F) of Fog. (A-B') non-transfected
671 S2 cells. (C-D') Mist-transfected S2 cells. (E-F') Smog-transfected S2 cells. A-F, phase
672 contrast; A'-F', merged images of phase contrast and V5 signals for transfected cells
673 (green). White arrowhead in E', Smog- transfected S2 cell is not contracting in the
674 absence of Fog. Magenta arrowheads, contracting cells. (G) Quantification of
675 percentage of contracting cells. n=~100 cells per condition from three independent
676 experiments. ****p≤0.0001 (Two-way ANOVA with Tukey's multiple comparison post
677 hoc analysis).

678

679 **Figure 3. *smog* knockdown and loss result in apical constriction defects in the SG**
680 **and disrupted epithelial morphology.** (A-F) Confocal images of SGs in control (A),
681 with zygotic knockdown of *smog* by using *TRiP.HMC03192* (B), with M/Z knockdown of
682 *smog* by using *TRiP.GL01473* (C), WT (D), *smog* null [mild] (E), and *smog* null [severe]
683 (F). (A'-F') Cell segmentation based on apical areas of A-F. Red and white lines, SG
684 boundary. Asterisks, invagination pit. (G, H) Quantification of percentage (left) and
685 cumulative percentage (right) of cells with different apical areas. Mann-Whitney U test
686 (for percentage of cells) and Kolmogorov-Smirnov test (for cumulative percentage of
687 cells). n=8 SGs (control, 902 cells; *smog* RNAi (Z), 823 cells; *smog* RNAi (M/Z), 881
688 cells; WT, 892 cells; *smog* null [mild], 859 cells); 6 SGs (*smog* null [severe], 672 cells); 5
689 SGs (*fog* mutant, 420 cells). ***p<0.001; ****p<0.0001. (I-L) 3D reconstruction of
690 confocal z-sections of SGs using Imaris for WT (I), M/Z knockdown of *smog* (J), *smog*
691 null [mild] (K), and *smog* null [severe] (L). Green, E-Cad. Magenta, CrebA. Asterisks,
692 invagination pit. Arrows in J and L, exaggerated grooves. Arrowheads in J and L,
693 enlarged SG cells. (M, N) Tile scan confocal images of stage 11 embryos in WT (M) and
694 M/Z knockdown of *smog* (N). Green, E-Cad. Magenta, CrebA. Arrows, ventral midline.
695 Arrowheads, SG.

696

697 **Figure 4. *smog* regulates all three pools of myosin in the SG in a Fog-dependent**
698 **and -independent manner.** (A-D'') Confocal images of SGs with sqh-GFP (green) and

699 E-Cad (magenta) signals. Compared to control (A-A''), sqh-GFP signals are dispersed
700 in SGs with zygotic (B-B'') and M/Z (C-C'') knockdown of *smog* and in *smog* null [mild]
701 embryos (D-D''). (A'-D'') Higher magnification of the yellow boxed region in A-D. (E-H'')
702 Confocal images of SGs with Rok-GFP (green) and E-Cad (magenta) signals.
703 Compared to control (E-E''), Rok-GFP signals are dispersed in SGs with zygotic (F-F'')
704 and M/Z (G-G'') knockdown of *smog* and in *smog* null [mild] embryos (H-H''). (E'-H")
705 Magnified images of the yellow boxed region in E-H. (I-L) Quantification of apicomedial
706 myosin intensity (I), junctional myosin intensity (J), area of apicomedial myosin particles
707 (K), and area of Rok-GFP particles (L). *p≤0.05; **p≤0.01; ***p≤0.001; ****p≤0.0001
708 (Welch's t-test). n=5 SGs, 100 cells (I-K) and 5 SGs, 75 cells (L) for each genotype. (M)
709 Control SG with high myosin intensity at the placode boundary (arrowheads in insets in
710 M, M''). (N) *smog* null [severe] SGs have low myosin intensity. Arrowheads in insets in
711 N, N'', discontinuous myosin at the SG boundary. (O) Analysis of the circularity of the
712 SG placode boundary as a measure of smoothness and tension. An example of a WT
713 SG stained for E-Cad (magenta) and sqh-GFP (green) with the boundaries measured.
714 Red line, SG boundary; gray line, cell boundary one cell row outside the SG boundary;
715 blue line, cell boundary one cell row inside the SG boundary. (P) Quantification of
716 circularity of the SG, outer, and inner boundary in control and *smog* null [severe] SGs.
717 Asterisks, invagination pit. *p≤0.05; **p≤0.01; ***p≤0.001 (Welch's t-test). n=5 SGs for
718 each genotype.
719
720 **Figure 5. Smog is required for maintaining epithelial integrity and the microtubule**
721 **networks.** (A-D) Confocal images of stage 11 WT (A, C) and *smog* null [severe] (B, D)
722 embryos (A, B) Embryos stained for E-Cad (green) and CrebA (magenta). (A', B')
723 Magnified view of the white boxed region in A and B. Compared to uniform and
724 continuous E-Cad signals in WT embryonic epithelial cells (A'), E-Cad signals are
725 absent in regions of epithelial cells in *smog* mutants (arrowheads in B'). (C, D) Embryos
726 stained for Crb (green) and CrebA (magenta). (C', D') magnified view of the white box
727 region in C and D. In contrast to continuous WT Crb signals (C'), Crb is almost absent in
728 regions of epithelial cells in *smog* mutants (arrowheads in D'). (E-J) E-Cad (E-G) and

729 Crb (H-J) signals in WT (E, H), *smog* null [mild] (F, I), and *smog* null [severe] (G, J)
730 embryos. Insets, magnified view of yellow boxed region in the SG. Arrowheads, gaps in
731 E-Cad or Crb signals. (K-N) Quantification of the number of gaps in E-Cad (K) and Crb
732 (M) signals and the ratio of gap length to total junctional length for E-Cad (L) and Crb
733 (N). n=5 SGs, 50 cells per genotype. **p≤0.01; ***p≤0.001 (Welch's t-test). (O-R)
734 Compared to WT (O, Q), acetylated tubulin signals are almost absent in the SG in *smog*
735 mutants (P), and tyrosinated tubulin signals are also reduced in *smog* mutants (R). Red
736 dotted lines, SG boundary. (S) Quantification of the ratio of tyrosinated tubulin intensity
737 in SG cells to the intensity in cells outside the SG placode. n=4 SGs (control); 5 SGs
738 (*smog* null). *p≤0.05 (Welch's t-test). Asterisks, invagination pit.
739
740 **Figure 6. Smog is required for maintaining cortical actin networks during SG**
741 **invagination.** (A-B''') Rok-GFP (green) and E-Cad (magenta) in SGs in control (A-A''')
742 and *smog* null [severe] (B-B''') embryos. (A'-B'') Higher magnification of the white boxed
743 regions in A and B. (A''', B''') x-z sections across the yellow lines in A and B. Red
744 arrowheads, normal Rok-GFP signals accumulated in the apicomedial region of control
745 SG cells. White arrowheads, blebs in SG cells in *smog* mutants enriched with Rok-GFP
746 signals. (C, D) SGs stained for Dia (green) and phalloidin (magenta) in WT (C) and
747 *smog* null mutant (D) embryos. Compared to high intensity of Dia (red arrowheads in C,
748 C'') and phalloidin (cyan arrowheads in D, D'') in the WT SG, Dia and phalloidin signals
749 are reduced in SGs in *smog* null mutants (red and cyan arrowheads in D-D''). (E-G)
750 Quantification of Dia intensity in apicomedial (E) and junctional (F) regions and the ratio
751 of apicomedial to junctional Dia intensity (G). (H-I'') Rok-GFP (green) and E-Cad
752 (magenta) in *chic* RNAi in the wild-type (H-H'') and *smog* mutant background (I-I''). (H'-
753 I'') Higher magnification of the white boxed regions in H, I. In *chic* RNAi SGs, Rok-GFP
754 signals accumulate in the apicomedial region of SG cells (red arrowheads in H' and H'').
755 *smog* null [mild] SG cells with *chic* knockdown show membrane blebs with enriched
756 Rok-GFP signals (white arrowheads in I' and I''). Asterisks, invagination pit. *p≤0.05;
757 **p≤0.01 (Welch's t-test). n=5 SGs, 50 cells for each genotype.
758

759 **Figure 7. A proposed model for roles of Smog during epithelial tube formation.**
760 During SG invagination, Smog responds to Fog signal to promote Rok accumulation
761 and apicomedial myosin formation to control apical constriction (red arrows).
762 Independent of Fog (and responding to an as-yet-unknown ligand X), Smog regulates
763 epithelial integrity by regulating junctional and the supracellular myosin pools, the
764 microtubule networks, and key apical/junctional components (grey arrows). Smog is
765 also required for cortical actin organization during SG invagination, through regulating
766 Dia levels (grey arrows). Different ligands may recruit specific G proteins and RhoGEFs
767 to activate distinct downstream effectors.
768
769 **Supplementary Figure S1. *smog* knockdown using a weaker RNAi line also shows**
770 **apical constriction defects in SG cells.** (A, A') A representative confocal image (A) of
771 the stage 11 SG in *fog* mutants and the corresponding heat map of apical areas (A').
772 The embryo surface is often uneven in *fog* mutant embryos due to additional folding and
773 grooves, resulting in some cells outside the SG being out of focus and not shown in the
774 image. (B-C') Confocal images of SGs in control (B) and zygotic knockdown of *smog* by
775 using *TRiP.GL01473* (C) and corresponding heat maps of apical areas (B' and C'). Red
776 and white lines, SG boundary. Asterisks, invagination pit. (D) Quantification of
777 percentage and cumulative percentage of cells with different apical areas. Mann-
778 Whitney U test (for percentage of cells) and Kolmogorov-Smirnov test (for cumulative
779 percentage of cells). n=8 SGs (control, 902 cells; *smog* RNAi (Z), 856 cells). **$p \leq 0.01$.
780
781 **Supplementary Figure S2. SGs in *smog* null mutants have relatively normal**
782 **morphology at stage 14 and later during embryogenesis.** (A, B) Confocal images of
783 stage 15 WT (A) and *smog* null embryos stained for E-Cad (green) and CrebA
784 (magenta). (C-G) SGs stained for E-Cad in WT (C, E), *smog* M/Z knockdown (F), and
785 *smog* null mutant (D, G) embryos. All embryos at stage 14 and later have relatively
786 normal morphology, including the SG, excepto for a rare case of the crooked SG in
787 *smog* null mutants (D).
788

789 **Supplementary Figure S3. *smog* loss leads to the reduction of Crb levels in the**
790 **whole embryo and loss of Crb anisotropy at the SG boundary.** (A, B) Confocal
791 images of stage 14 WT (A) and *smog* null [severe] mutant (B) embryos stained for Crb
792 (green) and CrebA (magenta). (A', B') Magnified view of the white boxed region in A and
793 B. Compared to clear Crb signals at the cell boundary in WT (A'), Crb levels are
794 reduced and diffused in some *smog* null mutant embryos with a severely defective
795 morphology (B'). (C-H''') control (C-E''') and *smog* null [severe] embryos (F-H''')
796 showing sqh-mCh (green) and Crb (magenta) signals. (D, G) Cells at the SG boundary.
797 (E, H) SG cells near the invagination pit (asterisk). (D'-H''') Higher magnification of the
798 boxed regions. In contrast to high myosin (red arrowheads in D''') and low Crb (cyan
799 arrowheads in D'') levels in the SG boundary in control embryos, the overall Crb levels
800 are reduced in *smog* null embryos, showing loss of anisotropic localization of Crb at the
801 SG boundary (G-H''').
802
803 **Supplementary Figure S4. *smog* loss leads to bleb formation in SG cells as well**
804 **as outside the SG placode.** (A-C'') Confocal images for Rok-GFP (green) and E-Cad
805 (magenta) signals in stage 11 SGs in control (A-A''), *smog* null [mild] (B-B''), and *fog*
806 mutant (C-C'') embryos. Blebs are not observed in these embryos. Due to the uneven
807 embryo surface in *fog* mutants, apical/junctional and more basal regions are shown for
808 SG cells near and far from the invagination pit, respectively, in the single z section. (D-
809 E'') Confocal images for Rok-GFP signals in control (D-D'') and *smog* null [severe] (E-
810 E'') embryos. Blebs are observed both in non-SG cells outside the SG placode (red
811 arrowheads in E') and SG cells (cyan arrowheads in E''). Yellow arrowheads in D'',
812 normal Rok accumulation in the apicomedial region of SG cells. Asterisk, invagination
813 pit.
814

815 **References**

816 **Abreu-Blanco, M. T., Verboon, J. M. and Parkhurst, S. M.** (2014). Coordination of Rho Family
817 GTPase Activities to Orchestrate Cytoskeleton Responses during Cell Wound Repair.
818 *Current Biology* **24**, 144–155.

819 **Afshar, K., Stuart, B. and Wasserman, S. A.** (2000). Functional analysis of the Drosophila
820 diaphanous FH protein in early embryonic development. *Development (Cambridge,*
821 *England)* **127**, 1887–97.

822 **Andrew, D. J. and Ewald, A. J.** (2010). Morphogenesis of epithelial tubes: Insights into tube
823 formation, elongation, and elaboration. *Developmental Biology* **341**, 34–55.

824 **Aoki, K., Maeda, F., Nagasako, T., Mochizuki, Y., Uchida, S. and Ikenouchi, J.** (2016). A
825 RhoA and Rnd3 cycle regulates actin reassembly during membrane blebbing. *Proceedings*
826 *of the National Academy of Sciences* **113**, E1863–E1871.

827 **Barrett, K., Leptin, M. and Settleman, J.** (1997). The Rho GTPase and a Putative RhoGEF
828 Mediate a Signaling Pathway for the Cell Shape Changes in Drosophila Gastrulation. *Cell*
829 **91**, 905–915.

830 **Benton, M. A., Frey, N., Nunes da Fonseca, R., von Levetzow, C., Stappert, D., Hakeemi,**
831 **M. S., Conrads, K. H., Pechmann, M., Panfilio, K. A., Lynch, J. A., et al.** (2019). Fog
832 signaling has diverse roles in epithelial morphogenesis in insects. *eLife* **8**, e47346.

833 **Blanchard, G. B., Murugesu, S., Adams, R. J., Martinez-Arias, A. and Gorfinkiel, N.** (2010).
834 Cytoskeletal dynamics and supracellular organisation of cell shape fluctuations during dorsal
835 closure. *Development* **137**, 2743–2752.

836 **Booth, A. J. R., Blanchard, G. B., Adams, R. J. and Röper, K.** (2014). A Dynamic Microtubule
837 Cytoskeleton Directs Medial Actomyosin Function during Tube Formation. *Developmental*
838 *Cell* **29**, 562–576.

839 **Charras, G. T.** (2008). A short history of blebbing. *Journal of Microscopy* **231**, 466–478.

840 **Charras, G. T., Yarrow, J. C., Horton, M. A., Mahadevan, L. and Mitchison, T. J.** (2005).
841 Non-equilibration of hydrostatic pressure in blebbing cells. *Nature* **435**, 365–369.

842 **Chung, S., Hanlon, C. D. and Andrew, D. J.** (2014). Building and specializing epithelial tubular
843 organs: the Drosophila salivary gland as a model system for revealing how epithelial organs
844 are specified, form and specialize. *WIREs Dev Biol* **3**, 281–300.

845 **Chung, S., Kim, S. and Andrew, D. J.** (2017). Uncoupling apical constriction from tissue
846 invagination. *eLife* **6**, e22235.

847 **Cooley, L., Verheyen, E. and Ayers, K.** (1992). chickadee encodes a profilin required for
848 intercellular cytoplasm transport during Drosophila oogenesis. *Cell* **69**, 173–184.

849 **Costa, M., Wilson, E. T. and Wieschaus, E.** (1994). A putative cell signal encoded by the
850 folded gastrulation gene coordinates cell shape changes during Drosophila gastrulation. *Cell*
851 **76**, 1075–1089.
852 **Dawes-Hoang, R. E., Parmar, K. M., Christiansen, A. E., Phelps, C. B., Brand, A. H. and**
853 **Wieschaus, E. F.** (2005). *folded gastrulation* , cell shape change and the control of myosin
854 localization. *Development* **132**, 4165–4178.
855 **Fox, D. T. and Peifer, M.** (2007). Abelson kinase (Abl) and RhoGEF2 regulate actin
856 organization during cell constriction in *Drosophila*. *Development* **134**, 567–578.
857 **Garcia De Las Bayonas, A., Philippe, J. M., Lellouch, A. C. and Lecuit, T.** (2019). Distinct
858 RhoGEFs Activate Apical and Junctional Contractility under Control of G Proteins during
859 Epithelial Morphogenesis. *Current Biology* **29**, 3370-3385.e7.
860 **Girdler, G. C. and Röper, K.** (2014). Controlling cell shape changes during salivary gland tube
861 formation in Drosophila. *Seminars in Cell & Developmental Biology* **31**, 74–81.
862 **Goode, B. L. and Eck, M. J.** (2007). Mechanism and Function of Formins in the Control of Actin
863 Assembly. *Annual Review of Biochemistry* **76**, 593–627.
864 **Gorfinkiel, N. and Blanchard, G. B.** (2011). Dynamics of actomyosin contractile activity during
865 epithelial morphogenesis. *Current Opinion in Cell Biology* **23**, 531–539.
866 **Guglielmi, G., Barry, J. D., Huber, W. and de Renzis, S.** (2015). An Optogenetic Method to
867 Modulate Cell Contractility during Tissue Morphogenesis. *Developmental cell* **35**, 646–660.
868 **Häcker, U. and Perrimon, N.** (1998). *DRhoGEF2* encodes a member of the Dbl family of
869 oncogenes and controls cell shape changes during gastrulation in *Drosophila*. *Genes &*
870 *Development* **12**, 274–284.
871 **Henderson, K. D. and Andrew, D. J.** (2000). Regulation and Function of Scr, exd, and hth in
872 the Drosophila Salivary Gland. *Developmental Biology* **217**, 362–374.
873 **Homem, C. C. F. and Peifer, M.** (2008). Diaphanous regulates myosin and adherens junctions
874 to control cell contractility and protrusive behavior during morphogenesis. *Development* **135**,
875 1005–1018.
876 **Izquierdo, E., Quinkler, T. and de Renzis, S.** (2018). Guided morphogenesis through
877 optogenetic activation of Rho signalling during early Drosophila embryogenesis. *Nature*
878 *Communications* **9**, 2366.
879 **Jha, A., van Zanten, T. S., Philippe, J.-M., Mayor, S. and Lecuit, T.** (2018). Quantitative
880 Control of GPCR Organization and Signaling by Endocytosis in Epithelial Morphogenesis.
881 *Current Biology* **28**, 1570-1584.e6.

882 **Jodoin, J. N., Coravos, J. S., Chanet, S., Vasquez, C. G., Tworoger, M., Kingston, E. R.,**
883 **Perkins, L. A., Perrimon, N. and Martin, A. C.** (2015). Stable Force Balance between
884 Epithelial Cells Arises from F-Actin Turnover. *Developmental Cell* **35**, 685–697.
885 **Kanesaki, T., Hirose, S., Grosshans, J. and Fuse, N.** (2013). Heterotrimeric G protein
886 signaling governs the cortical stability during apical constriction in Drosophila gastrulation.
887 *Mechanisms of Development* **130**, 132–142.
888 **Kerridge, S., Munjal, A., Philippe, J.-M., Jha, A., de las Bayonas, A. G., Saurin, A. J. and**
889 **Lecuit, T.** (2016). Modular activation of Rho1 by GPCR signalling imparts polarized myosin
890 II activation during morphogenesis. *Nature Cell Biology* **18**, 261–270.
891 **Kim, H. Y., Varner, V. D. and Nelson, C. M.** (2013). Apical constriction initiates new bud
892 formation during monopodial branching of the embryonic chicken lung. *Development* **140**,
893 3146–3155.
894 **Knirr, S., Azpiazu, N. and Frasch, M.** (1999). The role of the NK-homeobox gene slouch (S59)
895 in somatic muscle patterning. *Development (Cambridge, England)* **126**, 4525–35.
896 **Ko, C. S., Tserunyan, V. and Martin, A. C.** (2019). Microtubules promote intercellular
897 contractile force transmission during tissue folding. *Journal of Cell Biology* **218**, 2726–2742.
898 **Kölsch, V., Seher, T., Fernandez-Ballester, G. J., Serrano, L. and Leptin, M.** (2007). Control
899 of *Drosophila* Gastrulation by Apical Localization of Adherens Junctions and RhoGEF2.
900 *Science* **315**, 384–386.
901 **Le, T. P. and Chung, S.** (2021). Regulation of apical constriction via microtubule- and Rab11-
902 dependent apical transport during tissue invagination. *Molecular Biology of the Cell* **32**,
903 1033–1047.
904 **le Droguen, P.-M., Claret, S., Guichet, A. and Brodu, V.** (2015). Microtubule-dependent apical
905 restriction of recycling endosomes sustains adherens junctions during morphogenesis of the
906 *Drosophila* tracheal system. *Development* **142**, 363–374.
907 **Levayer, R. and Lecuit, T.** (2012). Biomechanical regulation of contractility: spatial control and
908 dynamics. *Trends in cell biology* **22**, 61–81.
909 **Lord, S. J., Velle, K. B., Mullins, R. D. and Fritz-Laylin, L. K.** (2020). SuperPlots:
910 Communicating reproducibility and variability in cell biology. *Journal of Cell Biology* **219**,
911 e202001064.
912 **Lubarsky, B. and Krasnow, M. A.** (2003). Tube morphogenesis: making and shaping
913 biological tubes. *Cell* **112**, 19–28.
914 **Manning, A. J. and Rogers, S. L.** (2014). The Fog signaling pathway: Insights into signaling in
915 morphogenesis. *Developmental Biology* **394**, 6–14.

916 **Manning, A. J., Peters, K. A., Peifer, M. and Rogers, S. L.** (2013). Regulation of Epithelial
917 Morphogenesis by the G Protein–Coupled Receptor Mist and Its Ligand Fog. *Science*
918 *Signaling* **6**, ra98.
919 **Martin, A. C. and Goldstein, B.** (2014). Apical constriction: themes and variations on a cellular
920 mechanism driving morphogenesis. *Development* **141**, 1987–1998.
921 **Martin, A. C., Kaschube, M. and Wieschaus, E. F.** (2009). Pulsed contractions of an actin–
922 myosin network drive apical constriction. *Nature* **457**, 495–499.
923 **Mason, F. M., Tworoger, M. and Martin, A. C.** (2013). Apical domain polarization localizes
924 actin–myosin activity to drive ratchet-like apical constriction. *Nature Cell Biology* **15**, 926–
925 936.
926 **Massarwa, R., Schejter, E. D. and Shilo, B.-Z.** (2009). Apical Secretion in Epithelial Tubes of
927 the Drosophila Embryo Is Directed by the Formin-Family Protein Diaphanous.
928 *Developmental Cell* **16**, 877–888.
929 **Munjal, A. and Lecuit, T.** (2014). Actomyosin networks and tissue morphogenesis.
930 *Development (Cambridge, England)* **141**, 1789–93.
931 **Myat, M. M. and Andrew, D. J.** (2000). Organ shape in the Drosophila salivary gland is
932 controlled by regulated, sequential internalization of the primordia. *Development*
933 *(Cambridge, England)* **127**, 679–91.
934 **Nikolaidou, K. K. and Barrett, K.** (2004). A Rho GTPase Signaling Pathway Is Used
935 Reiteratively in Epithelial Folding and Potentially Selects the Outcome of Rho Activation.
936 *Current Biology* **14**, 1822–1826.
937 **Parks, S. and Wieschaus, E.** (1991). The drosophila gastrulation gene concertina encodes a
938 Gα-like protein. *Cell* **64**, 447–458.
939 **Plageman, T. F., Chauhan, B. K., Yang, C., Jaudon, F., Shang, X., Zheng, Y., Lou, M.,**
940 **Debant, A., Hildebrand, J. D. and Lang, R. A.** (2011). A Trio-RhoA-Shroom3 pathway is
941 required for apical constriction and epithelial invagination. *Development* **138**, 5177–5188.
942 **Rao, M. V. and Zaidel-Bar, R.** (2016). Formin-mediated actin polymerization at cell–cell
943 junctions stabilizes E-cadherin and maintains monolayer integrity during wound repair.
944 *Molecular Biology of the Cell* **27**, 2844–2856.
945 **Romero, S., le Clainche, C., Didry, D., Egile, C., Pantaloni, D. and Carlier, M.-F.** (2004).
946 Formin Is a Processive Motor that Requires Profilin to Accelerate Actin Assembly and
947 Associated ATP Hydrolysis. *Cell* **119**, 419–429.
948 **Röper, K.** (2012). Anisotropy of Crumbs and aPKC Drives Myosin Cable Assembly during Tube
949 Formation. *Developmental Cell* **23**, 939–953.

Rousso, T., Shewan, A. M., Mostov, K. E., Schejter, E. D. and Shilo, B.-Z. (2013). Apical targeting of the formin Diaphanous in Drosophila tubular epithelia. *eLife* **2**, 1–19.

Royou, A., Field, C., Sisson, J. C., Sullivan, W. and Karess, R. (2004). Reassessing the Role and Dynamics of Nonmuscle Myosin II during Furrow Formation in Early *Drosophila* Embryos. *Molecular Biology of the Cell* **15**, 838–850.

Sanchez-Corrales, Y. E., Blanchard, G. B. and Röper, K. (2018). Radially patterned cell behaviours during tube budding from an epithelium. *eLife* **7**, e35717.

Shewan, A. M., Maddugoda, M., Kraemer, A., Stehbens, S. J., Verma, S., Kovacs, E. M. and Yap, A. S. (2005). Myosin 2 Is a Key Rho Kinase Target Necessary for the Local Concentration of E-Cadherin at Cell–Cell Contacts. *Molecular Biology of the Cell* **16**, 4531–4542.

Sidor, C., Stevens, T. J., Jin, L., Boulanger, J. and Röper, K. (2020). Rho-Kinase Planar Polarization at Tissue Boundaries Depends on Phospho-regulation of Membrane Residence Time. *Developmental Cell* **52**, 364-378.e7.

Sweeton, D., Parks, S., Costa, M. and Wieschaus, E. (1991). Gastrulation in Drosophila: the formation of the ventral furrow and posterior midgut invaginations. *Development (Cambridge, England)* **112**, 775–89.

Vázquez-Victorio, G., González-Espinosa, C., Espinosa-Riquer, Z. P. and Macías-Silva, M. (2016). GPCRs and actin–cytoskeleton dynamics. *Methods in Cell Biology* **132**, 165–188.

Weng, M. and Wieschaus, E. (2016). Myosin-dependent remodeling of adherens junctions protects junctions from Snail-dependent disassembly. *Journal of Cell Biology* **212**, 219–229.

Westermann, S. and Weber, K. (2003). Post-translational modifications regulate microtubule function. *Nature Reviews Molecular Cell Biology* **4**, 938–948.

Zweifel, M. E. and Courtemanche, N. (2020). Profilin's Affinity for Formin Regulates the Availability of Filament Ends for Actin Monomer Binding. *Journal of Molecular Biology* **432**, 166688.

Figure 1.

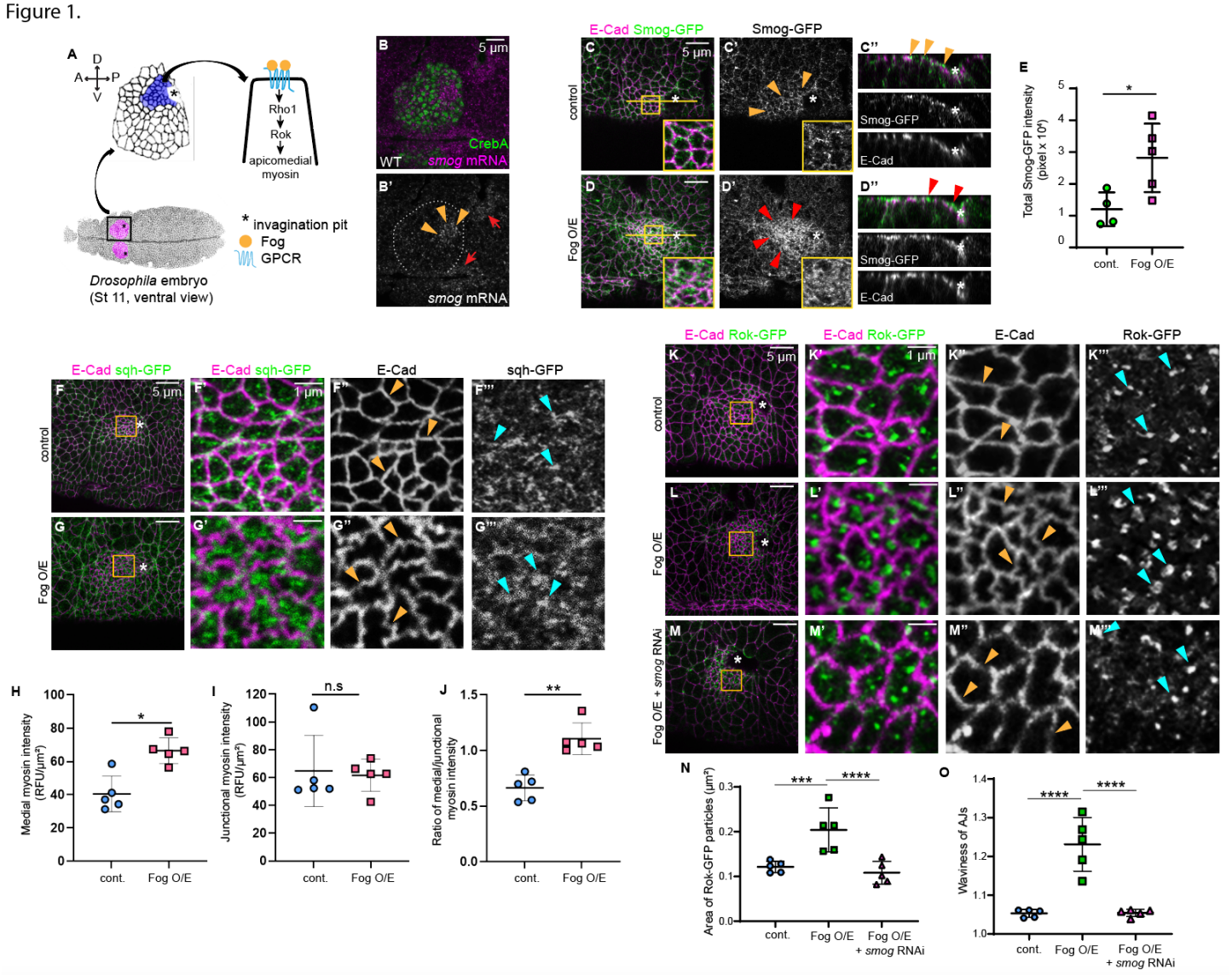
A
D
A
P
V
Rho1
Rok
apicomedial myosin
* invagination pit
Fog
GPCR
Drosophila embryo
(St 11, ventral view)
B
5 µm
CrebA
WT
smog mRNA
B'
smog mRNA
E-Cad Smog-GFP
Smog-GFP
control
Fog O/E
C
C'
C''
D
D'
D''
Smog-GFP
E-Cad
E
Total Smog-GFP intensity (pixel x 10⁴)
cont.
Fog O/E
E-Cad sqh-GFP
E-Cad
sqh-GFP
1 µm
F
F'
F''
F'''
G
G'
G''
G'''
H
Medial myosin intensity (RFU/µm²)
I
n.s
Junctional myosin intensity (RFU/µm²)
J
Ratio of medial/junctional myosin intensity
E-Cad Rok-GFP
Rok-GFP
4 µm
K
K'
K''
K'''
L
L'
L''
L'''
M
M'
M''
M'''
Fog O/E + smog RNAi
N
Area of Rok-GFP particles (µm²)
Fog O/E + smog RNAi
O
Waviness of AJs

Figure 2.

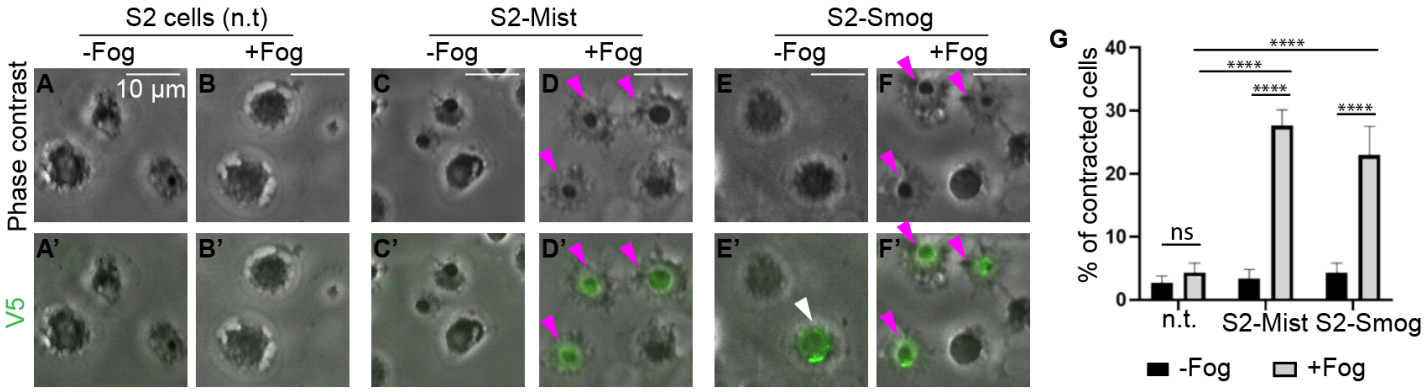
S2 cells (n.t)
S2-Mist
S2-Smog
-Fog
+Fog
Phase contrast
V5
10 µm
A
B
C
D
E
F
A'
B'
C'
D'
E'
F'
G
% of contracted cells
40
30
20
10
0
ns
****
n.t.
S2-Mist
S2-Smog
-Fog
+Fog

Figure 3.

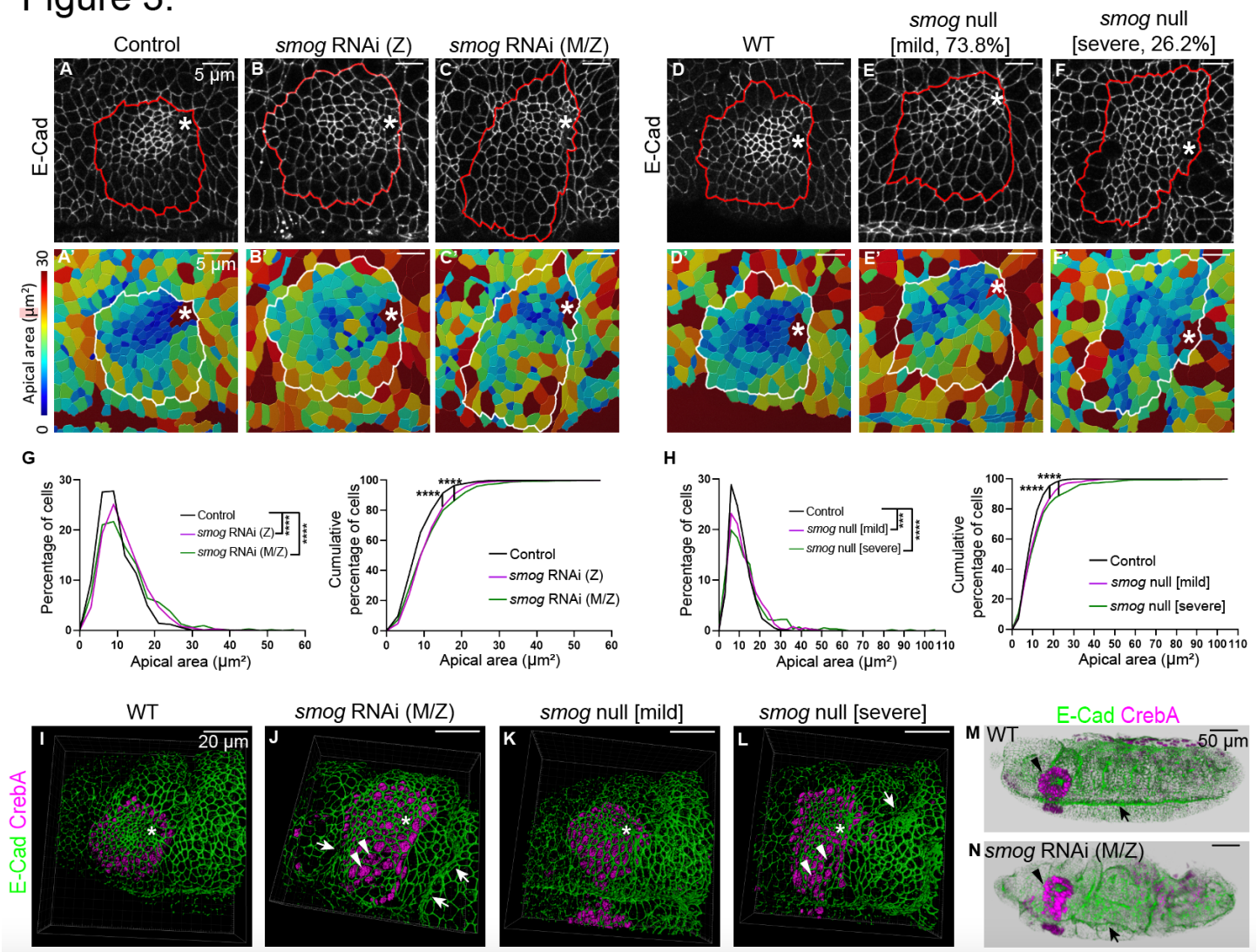
Control
smog RNAi (Z)
smog RNAi (M/Z)
WT
smog null [mild, 73.8%]
smog null [severe, 26.2%]
E-Cad
5 µm
Apical area (µm²)
G
H
Percentage of cells
Cumulative percentage of cells
Apical area (µm²)
Control
smog RNAi (Z)
smog RNAi (M/Z)
smog null [mild]
smog null [severe]
WT
smog RNAi (M/Z)
smog null [mild]
smog null [severe]
E-Cad CrebA
20 µm
50 µm

Figure 4.

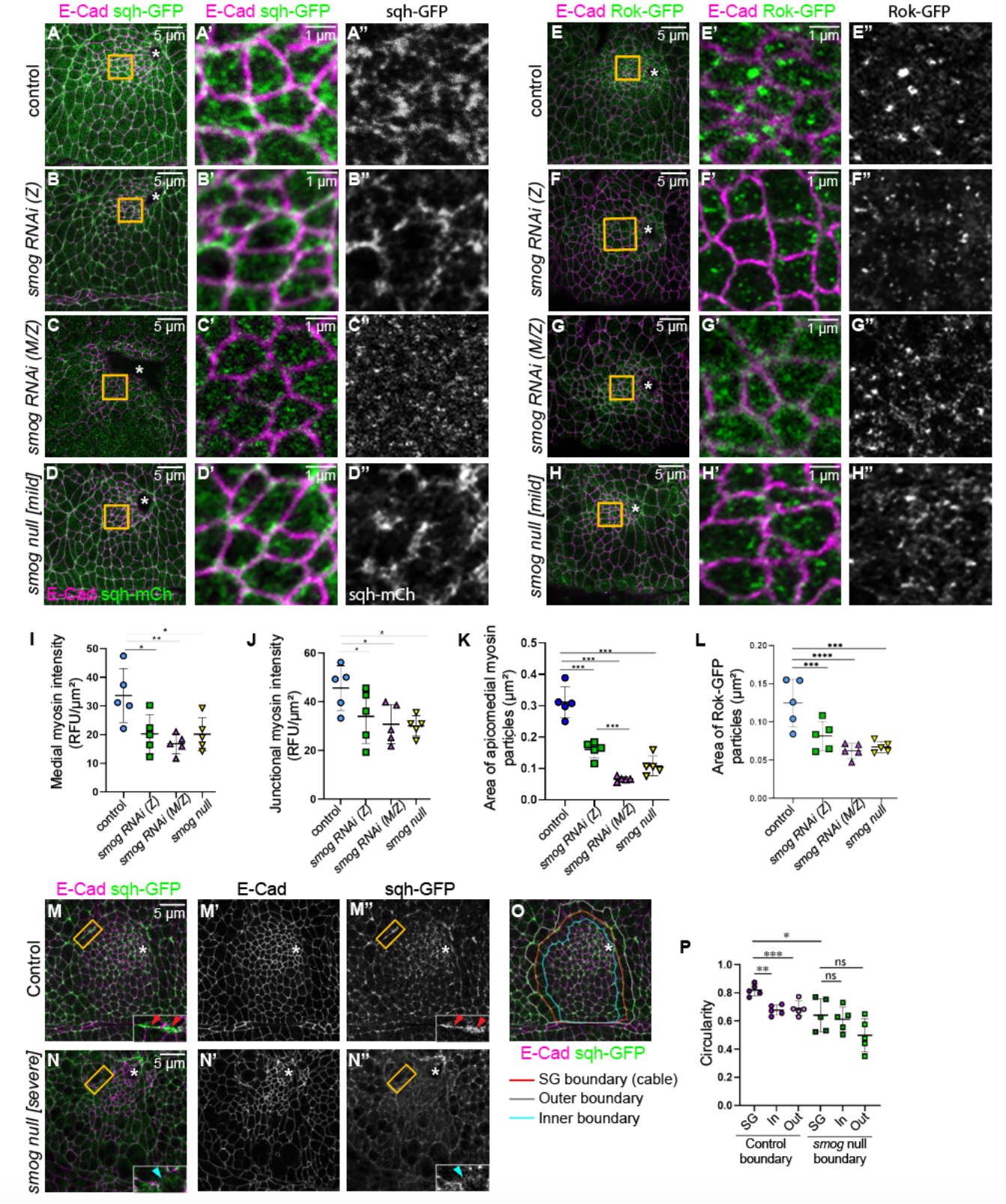
E-Cad sqh-GFP
E-Cad sqh-GFP
sqh-GFP
E-Cad Rok-GFP
E-Cad Rok-GFP
Rok-GFP
control
smog RNAi (Z)
smog RNAi (M/Z)
smog null [mild]
5 µm
1 µm
E-Cad sqh-mCh
sqh-mCh
Medial myosin intensity (RFU/µm²)
Junctional myosin intensity (RFU/µm²)
Area of apicomedial myosin particles (µm²)
Area of Rok-GFP particles (µm²)
control
smog RNAi (Z)
smog RNAi (M/Z)
smog null
E-Cad sqh-GFP
E-Cad
sqh-GFP
Control
smog null [severe]
E-Cad sqh-GFP
SG boundary (cable)
Outer boundary
Inner boundary
Circularity
SG
In
Out
Control boundary
smog null boundary
ns

Figure 5.

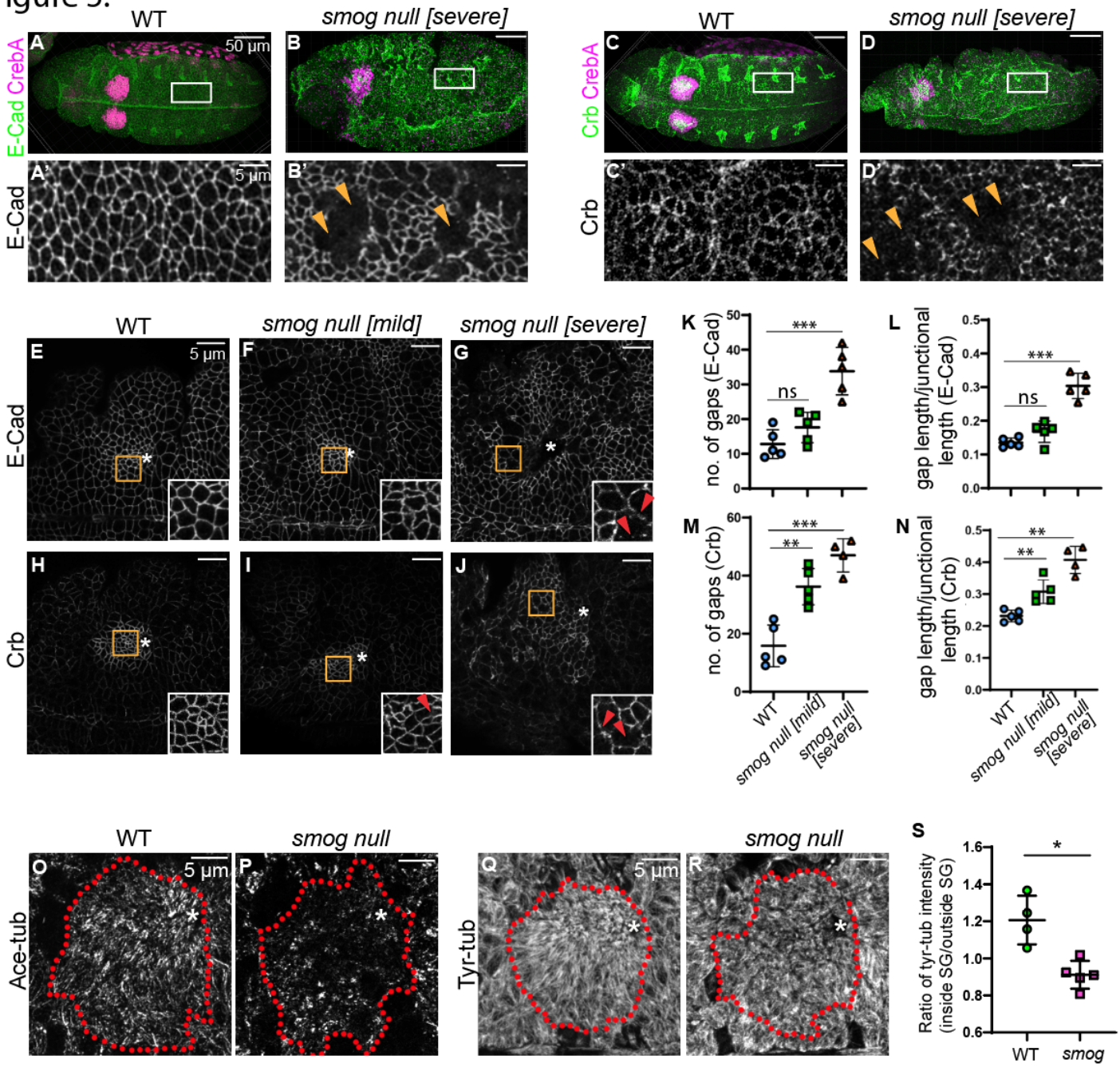
WT
smog null [severe]
E-Cad CrebA
A
50 µm
B
A'
5 µm
B'
E-Cad
WT
smog null [severe]
Crb CrebA
C
D
C'
D'
Crb
WT
smog null [mild]
smog null [severe]
E
5 µm
F
G
E-Cad
H
I
J
Crb
K
no. of gaps (E-Cad)
***
ns
L
gap length/junctional length (E-Cad)
***
ns
M
no. of gaps (Crb)
***
**
N
gap length/junctional length (Crb)
**
**
WT
smog null [mild]
smog null [severe]
WT
smog null
O
5 µm
P
Ace-tub
Q
5 µm
R
Tyr-tub
S
Ratio of tyr-tub intensity (inside SG/outside SG)
*
WT
smog

Figure 6.

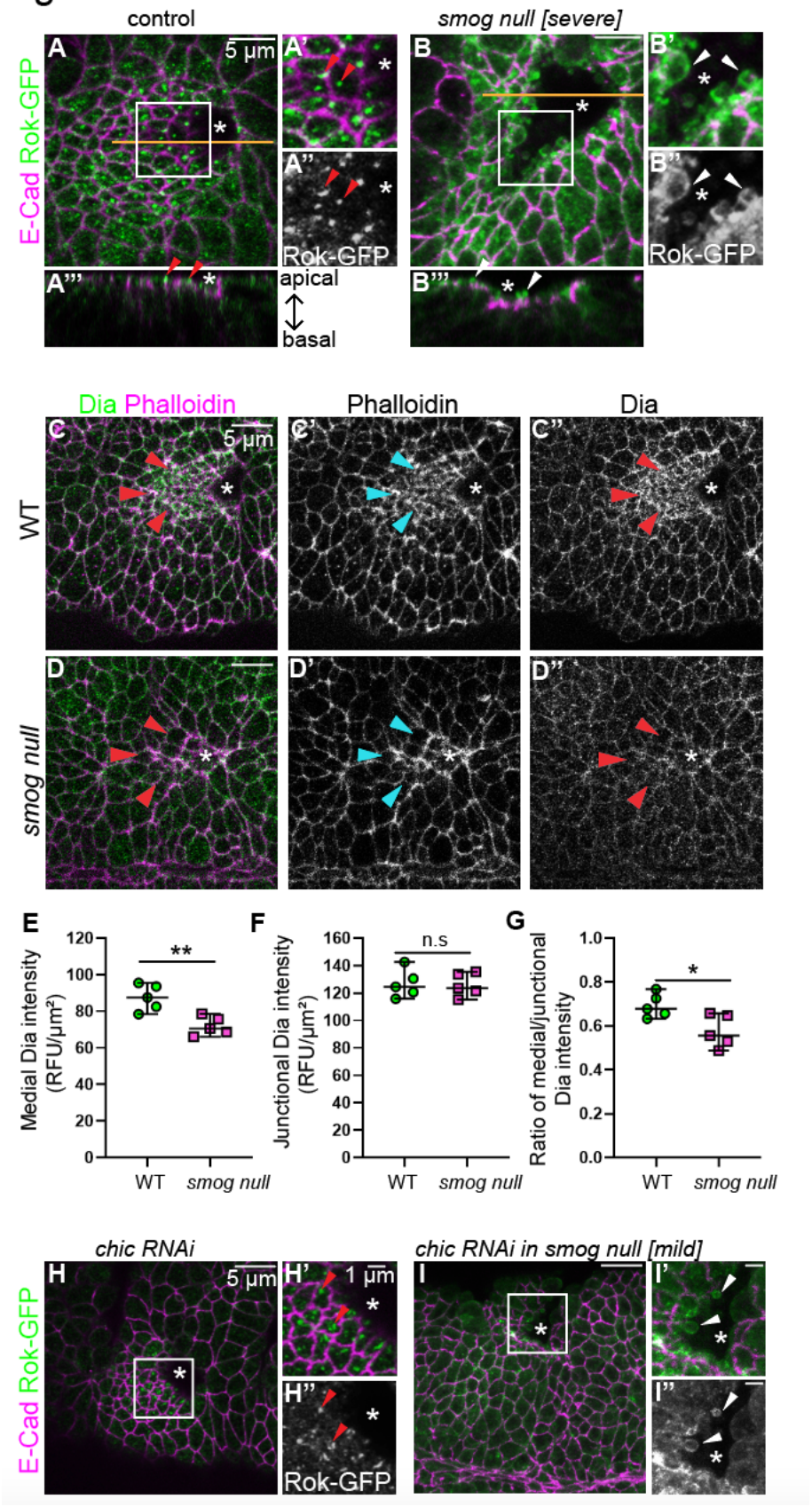
control
smog null [severe]
E-Cad Rok-GFP
5 µm
Rok-GFP
apical
basal
Dia Phalloidin
Phalloidin
Dia
WT
smog null
E
F
G
Medial Dia intensity (RFU/µm²)
Junctional Dia intensity (RFU/µm²)
Ratio of medial/junctional Dia intensity
**
n.s
*
WT
smog null
chic RNAi
chic RNAi in smog null [mild]
1 µm

Figure 7.

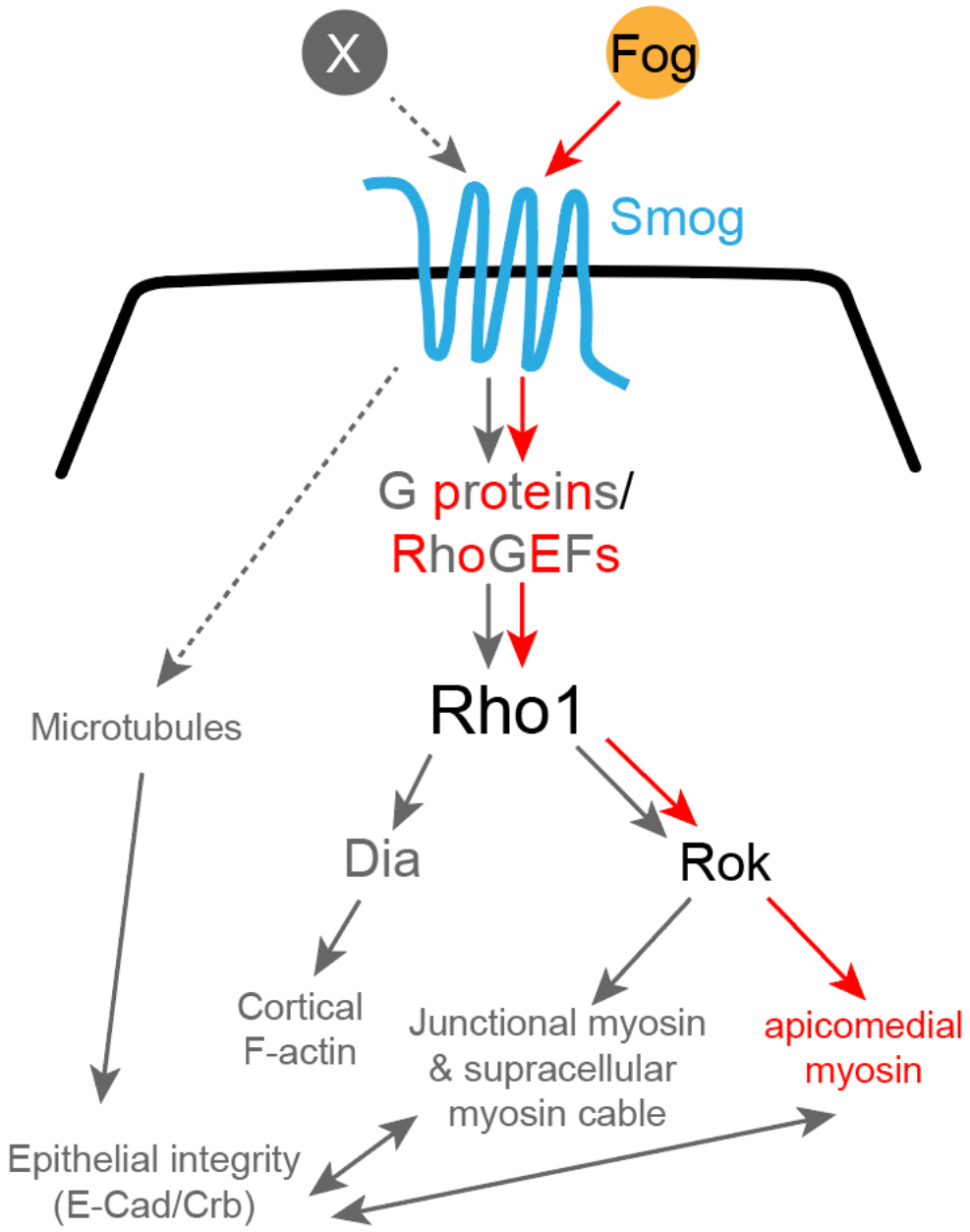
X
Fog
Smog
G proteins/
RhoGEFs
Rho1
Microtubules
Dia
Rok
Cortical
F-actin
Junctional myosin
& supracellular
myosin cable
apicomedial
myosin
Epithelial integrity
(E-Cad/Crb)

Sup. Fig. S1

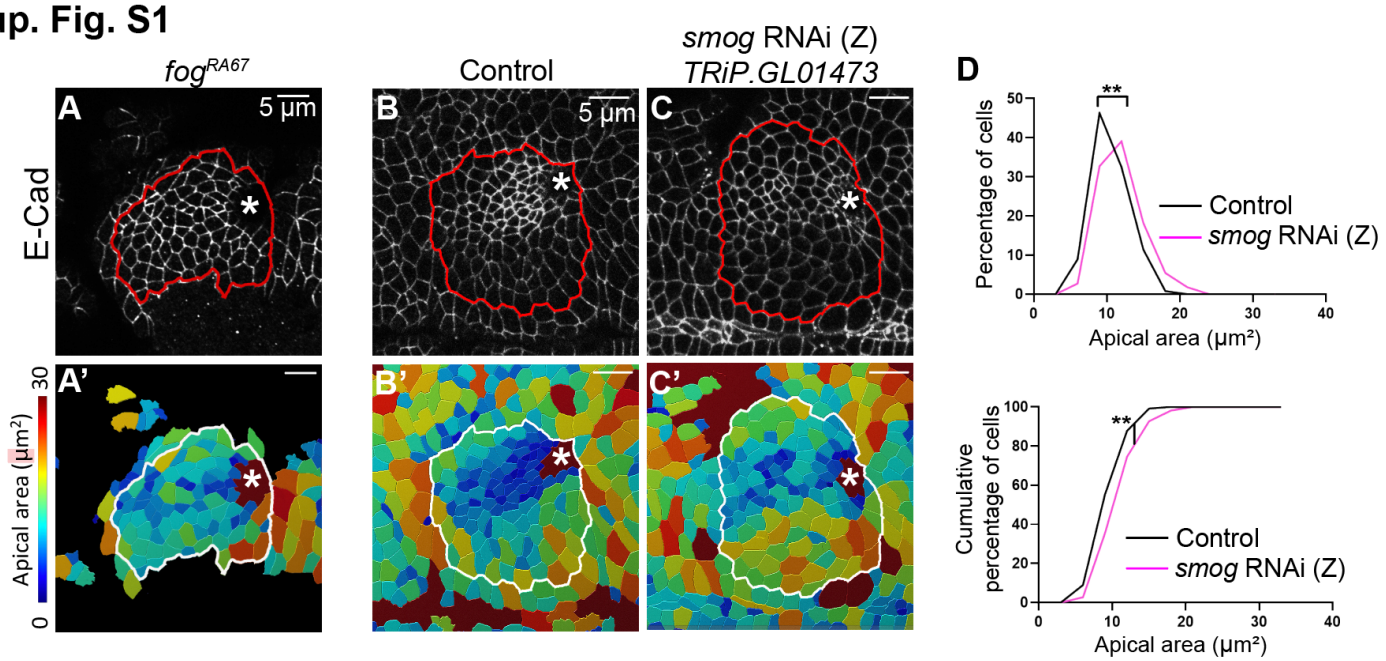
fogRA67
Control
smog RNAi (Z)
TRiP.GL01473
A
B
C
5 µm
5 µm
E-Cad
A'
B'
C'
Apical area (µm²)
30
0
D
Percentage of cells
Apical area (µm²)
Control
smog RNAi (Z)
**
Cumulative percentage of cells
Apical area (µm²)
Control
smog RNAi (Z)
**

Sup. Fig. S2

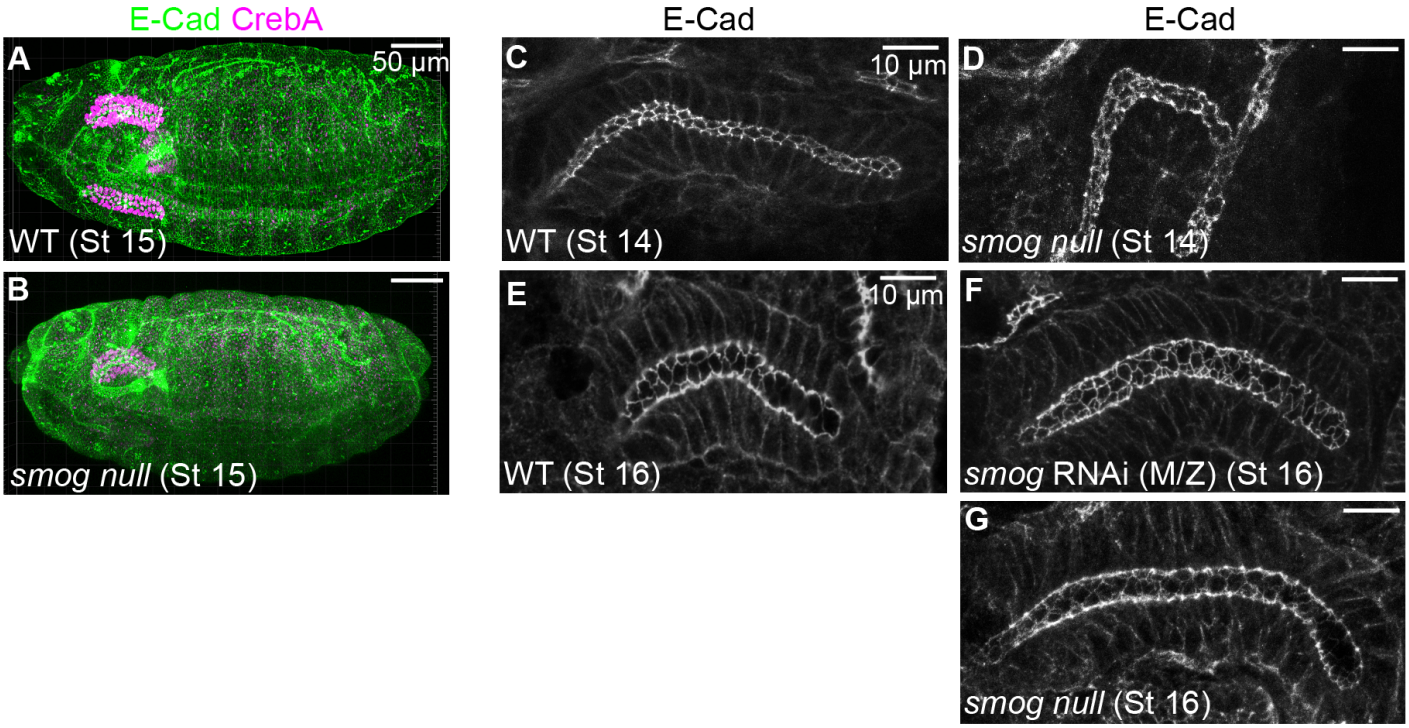
E-Cad CrebA
E-Cad
E-Cad
A
50 µm
WT (St 15)
B
smog null (St 15)
C
10 µm
WT (St 14)
D
smog null (St 14)
E
10 µm
WT (St 16)
F
smog RNAi (M/Z) (St 16)
G
smog null (St 16)

Sup. Fig. S3

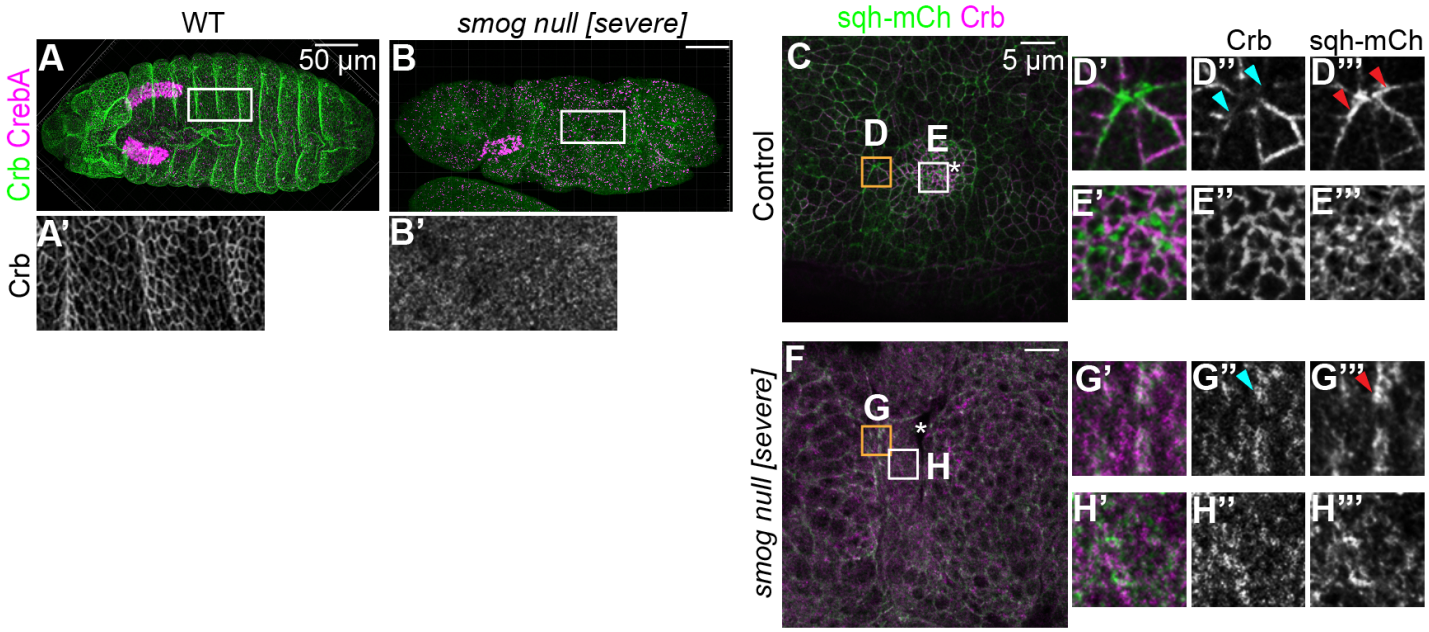
WT
smog null [severe]
Crb CrebA
A
50 µm
B
Crb
A'
B'
sqh-mCh Crb
C
5 µm
Control
D
E
*
Crb
sqh-mCh
D'
D''
D'''
E'
E''
E'''
F
smog null [severe]
G
*
H
G'
G''
G'''
H'
H''
H'''

Sup. Fig. S4

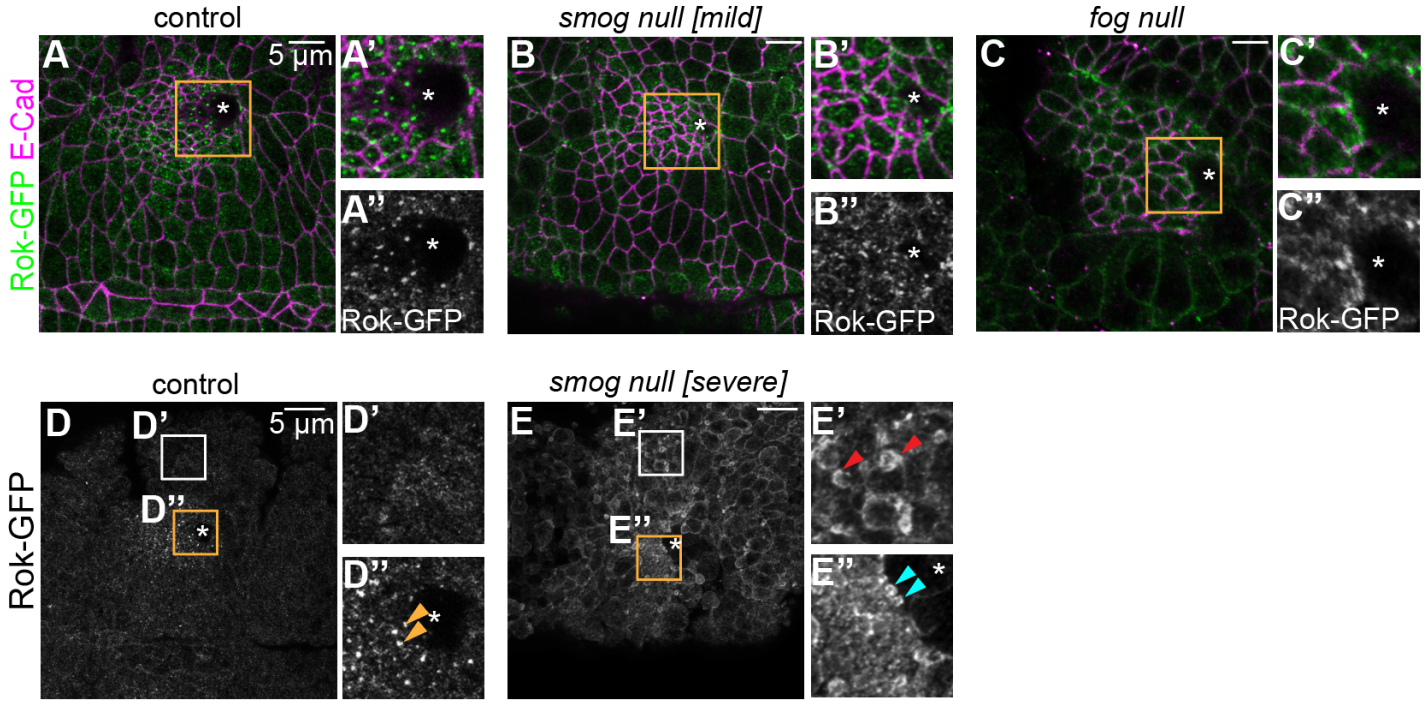
control
smog null [mild]
fog null
Rok-GFP E-Cad
A
5 µm
A'
A''
Rok-GFP
B
B'
B''
Rok-GFP
C
C'
C''
Rok-GFP
control
smog null [severe]
Rok-GFP
D
D'
D''
5 µm
E
E'
E''